

# The role of the free surface on interfacial solitary waves

G. la Forgia<sup>1</sup> and G. Sciortino<sup>2</sup>

<sup>1)</sup>*Institute of Marine Sciences, National Research Council, 00133, Rome, Italy<sup>a)</sup>*

<sup>2)</sup>*Department of Engineering, Roma Tre University, 00146, Rome, Italy*

(Dated: 8 September 2019)

We investigated theoretically and experimentally internal solitary waves (ISWs) in a two-layer fluid system with a top free surface. Laboratory experiments are performed by lock-release, under Boussinesq and non-Boussinesq conditions. Experimental results are compared with those obtained by the analytical solution of Korteweg-de Vries (KdV) weakly nonlinear equation, and by the strongly nonlinear Miyata-Choi-Camassa (MCC) model. We analyze the initial conditions which allow to find soliton solutions for both rigid-lid (-RL) and free-surface (-FS) boundary conditions. For the MCC-FS model, we employ a new mathematical procedure to derive the ISW-induced free surface displacement. The density structure strongly affects the elevation of the free surface predicted by the MCC-FS model. The free surface maximum displacement increases mostly with the density difference, assuming non-negligible values also for smaller interfacial amplitudes. Larger displacements occur for thinner upper layer thickness. The MCC-FS model gives the best prediction in terms of both internal waves geometric/kinematic features and surface displacements. The existence of a free surface allows the ISW to transfer part of its energy to the free surface: the wave celerity assumes lower values with respect to ISW speed resulting from the MCC-RL model. For ISWs with a very large amplitude, this behavior tends to fade, and the MCC-RL and the MCC-FS model predict approximately the same celerity and interfacial geometric features. For small-amplitude waves, also predictions of the KdV-RL equation are consistent with experimental results. Thus, ISWs with an intermediate amplitude should be modeled taking into account a free top surface as boundary condition.

<sup>a)</sup>Electronic mail: giovanni.laforgia@uniroma3.it.

## I. INTRODUCTION

Nonlinear internal solitary waves (ISWs) are widespread features of the global ocean. They propagate along a pycnocline, the layer of the water column with a strong, vertical density gradient, due to differences in water temperature or salinity between the surrounding waters<sup>1</sup>. They can be generated in a wide variety of ways, including by lee waves, tidal beams, resonance and river plumes<sup>2–6</sup>. However, ISWs of large amplitude are primarily generated by the action of tidal currents over bottom topography like sills, continental slopes, or sand banks<sup>7–9</sup>. ISWs generated in each tidal period tend to be grouped together into an ordered packets, with the largest wave in the lead<sup>10</sup>. The alteration of the sea surface roughness due to ISWs generation and propagation, make them readily detectable by satellite images. During the propagation of ISWs packets, convergent and divergent zones on the surface that move in phase with their troughs. These zones cause variations in sea surface roughness that appear as distinctive features in synthetic aperture radar (SAR)<sup>11</sup>.

ISWs can travel long distances, then they steepen due to non-linearity and disperse into trains of internal solitary waves and/or ultimately breaking along continental shelf/slope. These breaking waves can transport deep ocean water and associated constituents towards the continental margins and locally inducing sediment redistribution, turbulence and mixing, with important effects on near-shore ecosystems<sup>12,13</sup>. Breaking ISWs have been widely investigated in the past by non-analytical methods, such as laboratory experiments, numerical simulations and field observations<sup>14–16</sup>.

The oceanic observations have shown that the heights of the ISWs compared to the vertical scales of the stratification were large. Moreover, the fact that they preserve a finite amplitude for long distances implied that dispersion was not dominant, but rather it balanced the non-linearity during propagation. Nevertheless, weakly nonlinear theories have played the primary role in showing the essential features of the observations. The Korteweg-de Vries (*KdV*) equation was the canonical equation describing for the evolution of large amplitude ISWs. It considered the balance between the weakly nonlinear wave steepening and linear dispersion is the Korteweg-de Vries equation<sup>17</sup>. Following the *KdV* approach, the non-linearity is scaled by  $\alpha = a/h$  (i.e. ISW amplitude divide by the shallow water depth), while the non-hydrostatic dispersion is scaled by  $\beta = h/\lambda$  (where  $\lambda$  is the ISW wavelength), such that:  $\beta = O(\alpha) \ll 1$ . Comparing theoretical and experimental results, Grue *et al.*<sup>18</sup> showed that the *KdV* theory was relevant for small ISW amplitude but

## The role of the free surface on interfacial solitary waves

exhibited a systematic deviation from their laboratory experiments for amplitudes exceeding approximately 0.4 times the depth of the shallower (most commonly upper) layer. Useful upgrades of the  $KdV$  equation included higher-order non-linear and/or dispersive terms<sup>19</sup>. For example, the extended  $KdV$  ( $eKdV$ ) equation included cubic term which was  $O(\alpha^2)$ <sup>20</sup>. As the waves become narrower with increasing amplitudes, solitary wave solutions of  $eKdV$  and  $KdV$  models show crucial differences even for relatively small amplitudes. However, once the amplitude tends to a critical value, the  $ekdV$  solitary wave solution become inconsistent, generating large-amplitude "table-top" solitons<sup>21</sup>.

To accurately describe properties of oceanic observations of relatively large-amplitude ISWs, compared to the total water depth  $H$ , fully non-linear models have been employed. Fully nonlinear ISWs can be obtained by solving the Dureuil-Jacotin-Long (DJL) equation<sup>22</sup>, which is equivalent to the full set of the stratified Euler equations in the steady state. Since in the derivation of the DJL equation, no assumption with respect to the nonlinearity of the fluid flow is made, the resulting solutions are exact ISWs solutions in the inviscid limit. However, for non-constant buoyancy frequency, the DJL equation does not have analytical solutions but it has to be solved numerically<sup>23</sup>. The most recent analytical solution for fully non-linear ISWs was derived by Miyata<sup>24,25</sup>, Choi and Camassa<sup>26</sup>: a two-layer theoretical model ( $MCC$ ) considering full non-linearity (i.e.  $O(a/H) = 1$ ), and retaining only the weakly dispersive effects ( $\beta \ll 1$ ). Investigations over a wide range of stratified fluid domains proved that  $MCC$  solitary wave solutions are in good agreement with both laboratory experiments<sup>27,28</sup>, and observations<sup>29</sup>.

Both theoretical and experimental studies concerning with lock-release ISWs were performed in the past, mostly with the rigid-lid approximation or using a density difference too low to induce surface manifestations<sup>18,30–32</sup>. For the first time, Kodaira *et al.*<sup>33</sup> studied large-amplitude internal solitary waves propagating under the top free surface in a two-layer system of uniform densities. For a better understanding of the surface manifestations induced by ISWs, they allowed the top surface to be free when the interaction of internal solitary waves with relatively short surface waves. By using two immiscible fluids with a non-negligible density jump at the interface, they compared experimental results with those obtained by strongly nonlinear model ( $MCC$ ), under both the free surface (FS) and rigid-lid (RL) approximations. They performed a series of laboratory experiments in which they generate 5 ISWs by lock-release. They used increasing ratios between the interfacial displacement  $\eta$  and the shallow layer thickness  $h_1$  (within the range 0.6 – 3), in order to investigate how it affects the surface manifestations above ISWs.

## The role of the free surface on interfacial solitary waves

In the present work, we performed a series of 13 laboratory experiments in order to thoroughly investigate which parameters affect the surface manifestations induced by ISWs. We remark that our idealized experimental setting reproduce the physical processes involved in the real field, but it does not simulate real field geometries and conditions. By producing a large density difference as the one characterizing our initial setting, we indeed generated ISWs with visible and measurable surface displacements, in a small scale apparatus. We compared our results with those obtained using both weakly non-linear and fully non-linear theoretical models. We employed both the free surface and the rigid lid approximation at the top free surface. In particular, we derive for the *MCC-FS* model a new mathematical technique to obtain the free surface displacement for a given interfacial amplitude. Analytical processing is performed by Wolfram MATHEMATICA<sup>34</sup>. We deeply investigated how to properly set the initial conditions in order to solve the model equations. To better understand the role of the free surface on the overall flow features, we investigated theoretically a wide range of interfacial amplitudes up to the limiting values resulting *MCC* model.

In our experiments, we generated different waves by varying some initial setting parameters: the ratio  $\eta/h_1$  (from 1.4 to 34), the upper layer thickness within the ambient fluid, the initial surface displacement  $\delta_0$ . Moreover, we set different ratios  $\rho_1/\rho_2$ , from 0.72 to 0.81, obtaining both Boussinesq and quasi non-Boussinesq flow conditions. The latter have not yet been experimentally investigated in the past, at the best of our knowledge.

This paper is organized as follows. In Section II we describe the model equations for ISWs and their main features; Section III introduces the laboratory procedure adopted to generate different ISWs and associated surface manifestations; we analyze the experimental evidences, with particular mention to the observed surface manifestations, and the main parameters which affect flow features. Moreover, in Section IV we compare the experimental evidences and the models predictions. Finally, a general discussion and concluding remarks are inferred in Section V.

## II. MATHEMATICAL MODELS

### A. The *KdV* model for interfacial solitary waves

Let us consider a stratified system composed by two immiscible fluids whose uniform densities and thicknesses are given by  $\rho_i$  and  $h_i$  respectively, with  $i = 1$  for the upper fluid layer and  $i = 2$  for the lower layer (Fig. 1a). The spatio-temporal evolution of a weakly non-linear interfacial

# The role of the free surface on interfacial solitary waves

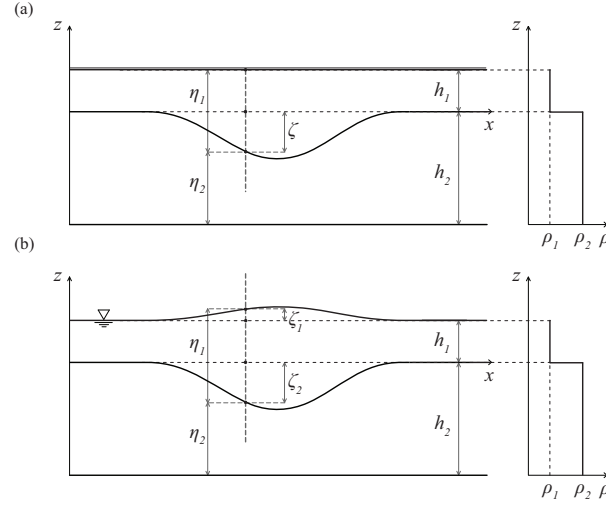


FIG. 1. Sketch of the density structure and the main geometric parameters defined to describe the surface and the interface displacements for (a) the rigid lid model and (b) the free surface model.

uni-directional wave, can be described by the Korteweg de Vries (*KdV*) equation<sup>35</sup>

$$\zeta_t + c_0 \zeta_x + c_1 \zeta \zeta_x + c_2 \zeta_{xxx} = 0, \quad (1)$$

where  $\zeta(x, t)$  is the interfacial vertical displacement. For weak non-linearity, this simplified model can be obtained by the the *MCC-RL* model with rigid lid assumption<sup>25,26</sup> and by the *MCC-FS* model with free surface assumption<sup>36,37</sup>.

The constant coefficients  $c_0, c_1, c_2$  in (1) depend on the densities  $\rho_i$  and thicknesses  $h_i$  of the two fluids at rest, although they are different for the two model *FS* and *RL*<sup>33</sup>. Homogeneous boundary conditions at infinity are considered to find soliton-solution to equation (1), with the form  $\zeta = \zeta(X)$ , where  $X \equiv x - ct$ . Looking for soliton-solution to equation (1) of the form  $\zeta = \zeta(X)$ , after some mathematical manipulations and taking into account homogeneous boundary conditions at infinity, the following first-order ordinary differential equation is obtained:

$$\zeta_X^2 = \frac{c_1}{3c_2} \zeta^2 (a - \zeta), \quad (2)$$

where  $c$  is the celerity of the *KdV* model, obtained as:

$$c = c_{KdV} \equiv c_0 + \frac{c_1 a}{3}. \quad (3)$$

This model requires that  $c_2 > 0$  and  $ac_1 > 0$  (see Eq. (2.22) and (2.23) in Kodaira *et al.*<sup>33</sup>), namely  $a$  and  $c_1$  have to be the same sign. This condition assures that the right side of Eq. (2) is positive

The role of the free surface on interfacial solitary waves

either for  $a > 0$  when  $0 < \zeta \leq a$  (solitary wave of elevation), or for  $a < 0$  when  $a \leq \zeta < 0$ .

It is important to note that the *KdV model* assures *soliton solutions* without implying limitations to the amplitude modulus<sup>38</sup>. Moreover, the right side of Eq. (2) shows a significant mathematical property: the polynomial cubic equation  $\zeta^2(a - \zeta) = 0$  has multiple roots (in this simple case  $\zeta = 0$ ), and consequently the *discriminant of the cubic equation must be zero*.

It easy to verify that the function:

$$\zeta(X) = \zeta(x - c_{KdV}t) \equiv a \text{Sech}^2(X/\lambda_{KdV}), \quad (4)$$

with  $\lambda_{KdV} \equiv \sqrt{12c_2/(ac_1)}$ , is an analytical *soliton solution* of the *KdV model*, namely it satisfies both the partial differential equation (1) and the ordinary first order non-linear differential equation (2).

## B. Rigid Lid Model

The rigid-lid model *MCC-RL*<sup>25,26</sup> assumes that the sum of the local thicknesses  $\eta_2$  and  $\eta_1$  within the heavier and lighter fluid, respectively, has to be constant and equal to the sum of the thicknesses at rest  $h_1 + h_2$  (Fig. 1a). As a consequence:

$$\eta_1 = h_1 - \zeta, \eta_2 = h_2 + \zeta, \quad (5)$$

where  $\zeta$  is the elevation of the separation surface.

To find a soliton solution, i.e. the unknowns depending on the variable  $X \equiv x - ct$ , from the continuity and momentum equations for each layer, the following non-linear differential equation in the  $\zeta = \zeta(X)$  unknown is derived<sup>33</sup>:

$$\zeta_X^2 = \frac{3\zeta^2(c^2(\rho_1\eta_2 + \rho_2\eta_1) - g(\rho_2 - \rho_1)\eta_1\eta_2)}{c^2(\rho_1h_1^2\eta_2 + \rho_2h_2^2\eta_1)}. \quad (6)$$

The right side of Eq. (6) is set to zero for  $\zeta = a$ , since the derivative of the interfacial profile  $\zeta(X)$  is zero at its maximum ( $a > 0$ ) or minimum ( $a < 0$ ). We thus obtain the wave-celerity as a function of the amplitude  $a$ :

$$c = c_{RL} \equiv \pm \sqrt{\frac{g(h_1 - a)(h_2 + a)(\rho_2 - \rho_1)}{\rho_1h_2 + a(\rho_1 - \rho_2) + \rho_2h_1}}. \quad (7)$$

For  $a \rightarrow 0$  the *MCC-RL* celerity becomes the so-called *linear-long-wave-celerity*:

$$c_{0,RL} \equiv \sqrt{\frac{gh_1h_2(\rho_2 - \rho_1)}{\rho_1h_2 + \rho_2h_1}}. \quad (8)$$



The role of the free surface on interfacial solitary waves

Unlike the *KdV* model, the rigid-lid approach implies the existence of a *limit-amplitude*  $A_{RL}$ . For  $A_{RL} > 0$  (soliton of elevation) the model does not admit solution for amplitude  $a > A_{RL}$ , while for  $A_{RL} < 0$  (soliton of depression) the model does not admit solution for amplitude  $a < A_{RL}$ . A simple mathematical approach to find  $A_{RL}$  is to look for the maximum of the celerity  $c_{RL}$  as a function of the amplitude  $a$ . Imposing the constraints  $h_1 - A_{RL} > 0$  and  $h_2 + A_{RL} > 0$ , i.e. the local thicknesses must be positive, we solve  $dc_{RL}/da = 0$  with respect to  $a$ . After some algebraic manipulations we obtain the analytical expression for  $A_{RL}$ :

$$A_{RL} = \frac{h_1 - h_2 \sqrt{\rho_1/\rho_2}}{1 + \sqrt{\rho_1/\rho_2}}. \quad (9)$$

Substituting  $a$  with  $A_{RL}$  in Eq. (7), the limit soliton celerity for the *MCC-RL* model is obtained:

$$C_{RL} = \pm \sqrt{g(h_1 + h_2) \frac{1 - \sqrt{\rho_1/\rho_2}}{1 + \sqrt{\rho_1/\rho_2}}}. \quad (10)$$

Relations (9) and (10) are equal to those shown in Kodaira *et al.*<sup>33</sup>. A consequence of (9) is that the *MCC-RL* model does not admit soliton solution when the condition  $h_1/h_2 = \sqrt{\rho_1/\rho_2}$  is fulfilled. Interestingly, setting equal to zero the right-hand of Eq. (6), a polynomial equation in the unknown  $\zeta$  is obtained. Owing to the factor  $\zeta^2$ , this equation has two coincident solutions  $\zeta = 0$ . Similarly to the *KdV* model (see Eq. (2)), the polynomial equation has *multiple roots*, thus it has zero as *discriminant*. This common feature of the considered mathematical models will be crucial to set the initial conditions for the more complex model *MCC-FS*, herein discussed. To integrate Eq. (6) it is necessary to substitute the expressions of both the celerity (Eq. (7)) and the local thicknesses (Eq. (5)). After some algebraic manipulation it is possible to obtain:

$$\zeta_X^2 = \frac{3(a - \zeta)\zeta^2((a + h_2)(h_2 + \zeta)\rho_1 + (a - h_1)(h_1 - \zeta)\rho_2)}{(a - h_1)(a + h_2)(h_1^2(h_2 + \zeta)\rho_1 + h_2^2(h_1 - \zeta)\rho_2)}, \quad (11)$$

where  $a$  is the wave amplitude (subject to the constraint  $|a| \leq |A_{RL}|$ ). The initial condition for this model is simply  $\zeta(0) = a$ . For a deeper understanding about the meaning of the wave amplitude limit value  $A_{RL}$ , some remarks are needed. Interestingly, if the amplitude-wave constraint  $|a| \leq |A_{RL}|$  is fulfilled, the-right side of Eq. (11) results always positive for  $|\zeta| < |a|$ , being the left-side equal to a square. This leads the differential equation to admit soliton solution. Otherwise, if  $|a| > |A_{RL}|$ , for some value of  $|\zeta| < |a|$  the right-side of Eq. (11) is negative and the model does not admits solutions, owing to  $\zeta_X^2$  cannot be negative.

## The role of the free surface on interfacial solitary waves

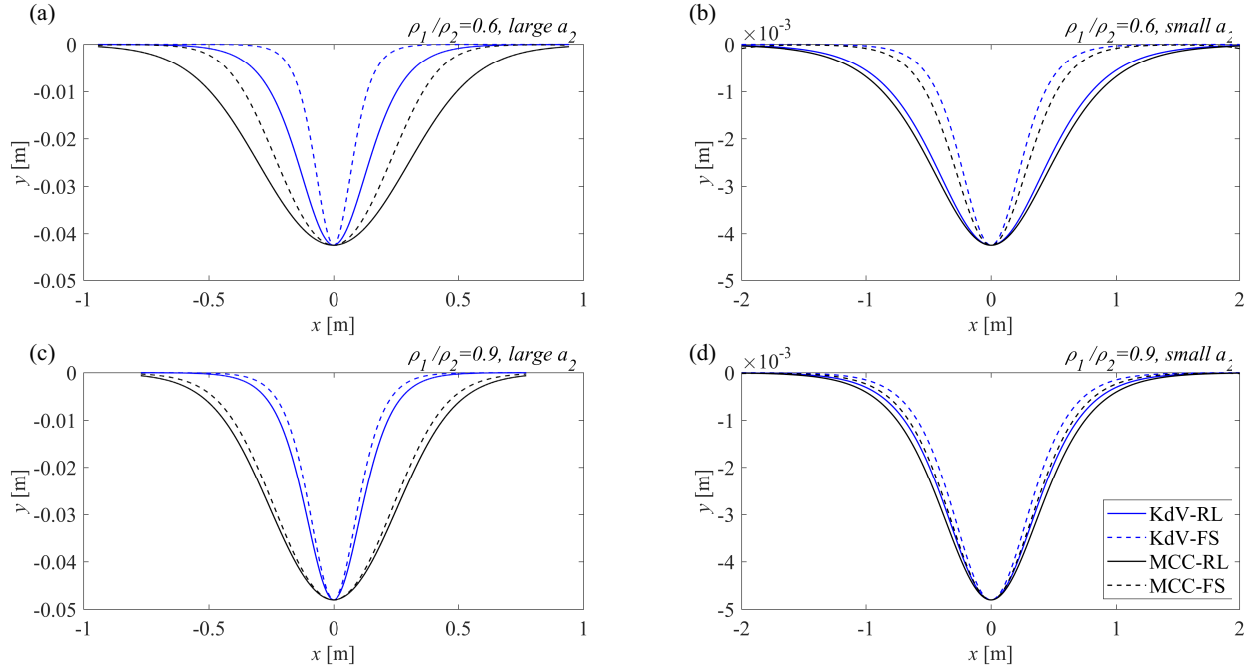


FIG. 2. ISW profiles predicted by both the *KdV* and the *MCC* model, considering the rigid lid approximation as well as the presence of a free surface. The two-fluid system is composed by  $h_1 = 0.05$  m and  $h_2 = 0.25$  m. The layers density is: (a,b)  $\rho_1/\rho_2 = 0.6$  and (c,d)  $\rho_1/\rho_2 = 0.9$ . Two conditions on wave amplitude are considered: (a,c) large amplitude, with  $a_2/h_1 \approx 1$ , and (b,d) small amplitudes, with  $a_2/h_1 \approx 0.1$ .

### C. Free surface model

The free-surface model *MCC-FS*, assumes the existence of a free surface and removes the rigid-lid assumption, namely that the sum of the local thicknesses  $\eta_1 + \eta_2$  has to be constant. With respect to the full water-wave problem, the associated truncation error has magnitude  $O(\frac{H}{\lambda})^4$ , where  $\lambda$  is the characteristic wavelength, and  $H = h_1 + h_2$  is the total water depth<sup>36,37</sup>. With this approach the relations of the interface and surface displacements  $\zeta_2$  and  $\zeta_1$ , respectively, with the local thicknesses  $\eta_1$  and  $\eta_2$  are defined as (Fig. 1b):

$$\begin{cases} \eta_1 = h_1 + \zeta_1 - \zeta_2 \\ \eta_2 = h_2 + \zeta_2 \end{cases} \quad (12)$$

We look for soliton solutions of the continuity and momentum equations for each layer (see Appendix, Eqs. A.1, A.2) of form  $\eta_i = \eta_i(X)$ ,  $u_i = u_i(X)$ ,  $X \equiv (x - ct)$  ( $i = 1, 2$ ). It is possible to show that  $u_i = c(1 - h_i/\eta_i)$ , obtaining the following *non-linear second order differential system*



The role of the free surface on interfacial solitary waves

of equations in the unknowns  $\eta_i(X)$ <sup>33</sup>:

$$\alpha_{j1}\eta_1'' + \alpha_{j2}\eta_2'' + \alpha_{j3}(\eta_1')^2 + \alpha_{j4}(\eta_2')^2 + \alpha_{j5}\eta_1'\eta_2' = \alpha_{j6}, \quad (13)$$

where  $j = 1, 2$  and the prime ( $'$ ) denotes derivative with respect to  $X$ . The coefficients  $\alpha_{ji}$  are non-linear functions of  $h_1, h_2, \eta_1, \eta_2, \rho_1, \rho_2$  and  $c$  (see Appendix, Eqs. A.3, A.4). To obtain the system (13), the third-order momentum equations (A.1) are integrated with respect to  $X$ , by using the following boundary conditions at infinity ( $\eta_i \rightarrow h_i, u_i \rightarrow 0$  as  $X \rightarrow \pm\infty$ ). From heavy non-linear differential manipulations of the continuity and momentum equations for each layer, it is possible to derive two other equations in conservation-law form, which represents the conservation of momentum and energy for the two-layers fluid system<sup>33</sup>. In terms of the unknowns  $\eta_i = \eta_i(X)$ , those equations can be expressed as in (13) but with another set of coefficients  $\alpha_{ji}$ , with  $j = 3, 4$ . A useful conserved quantity *Ham* (namely the Hamiltonian of the two-layers fluid system) of the differential equations (13) can be obtained as in Barros, Gavriluk, and Teshukov<sup>37</sup>. Once solved the system (13) with respect to the second derivatives  $\eta_1'', \eta_2''$ , those expressions are substituted into the conservation of momentum or energy ( $j = 3, 4$ , respectively). Then, after heavy algebraic manipulation, the following conserved quantity is obtained, which does not depend on second derivatives:

$$Ham = \beta_1(\eta_1')^2 + \beta_2(\eta_2')^2 + \beta_3\eta_1'\eta_2' + \beta_4, \quad (14)$$

where the coefficients  $\beta_j$  ( $j = 1, 2, 3, 4$ ) are defined in Appendix.

The numerical integration of the differential system (13) requires to define a suitable set of initial conditions in order to obtain soliton solutions. Barros and Gavriluk<sup>39</sup> addressed this issue by studying the existence of embedded solitary waves, corresponding to homoclinic orbits in the phase-space of the system. This can be achieved linearizing the system (13) in the neighborhood of the critical point  $(\eta_i, \eta_i') = (h_i, 0)$  and choosing suitable initial conditions from the analytical solutions of the linearized system. In particular, they assigned the initial conditions in order to stay as close as possible from the homoclinic orbit. They thus introduced a parameter  $k$  as a measure of the infinitesimal shift to it. It has to be *small enough* to ensure a suitable nearness to the critical solutions  $(\eta_i, \eta_i') = (h_i, 0)$ , since this point belongs to the homoclinic orbit. However, at the same time, it has to be *large enough* to avoid a great numerical precision for numerical integrations. This powerful technique requires, however, a series of attempts in order to obtain the sought solution, whose reliability strongly depends on the choice of the most appropriate  $k$ . The surface and the interfacial amplitudes are indeed *a posteriori* obtained i.e., after assigning the

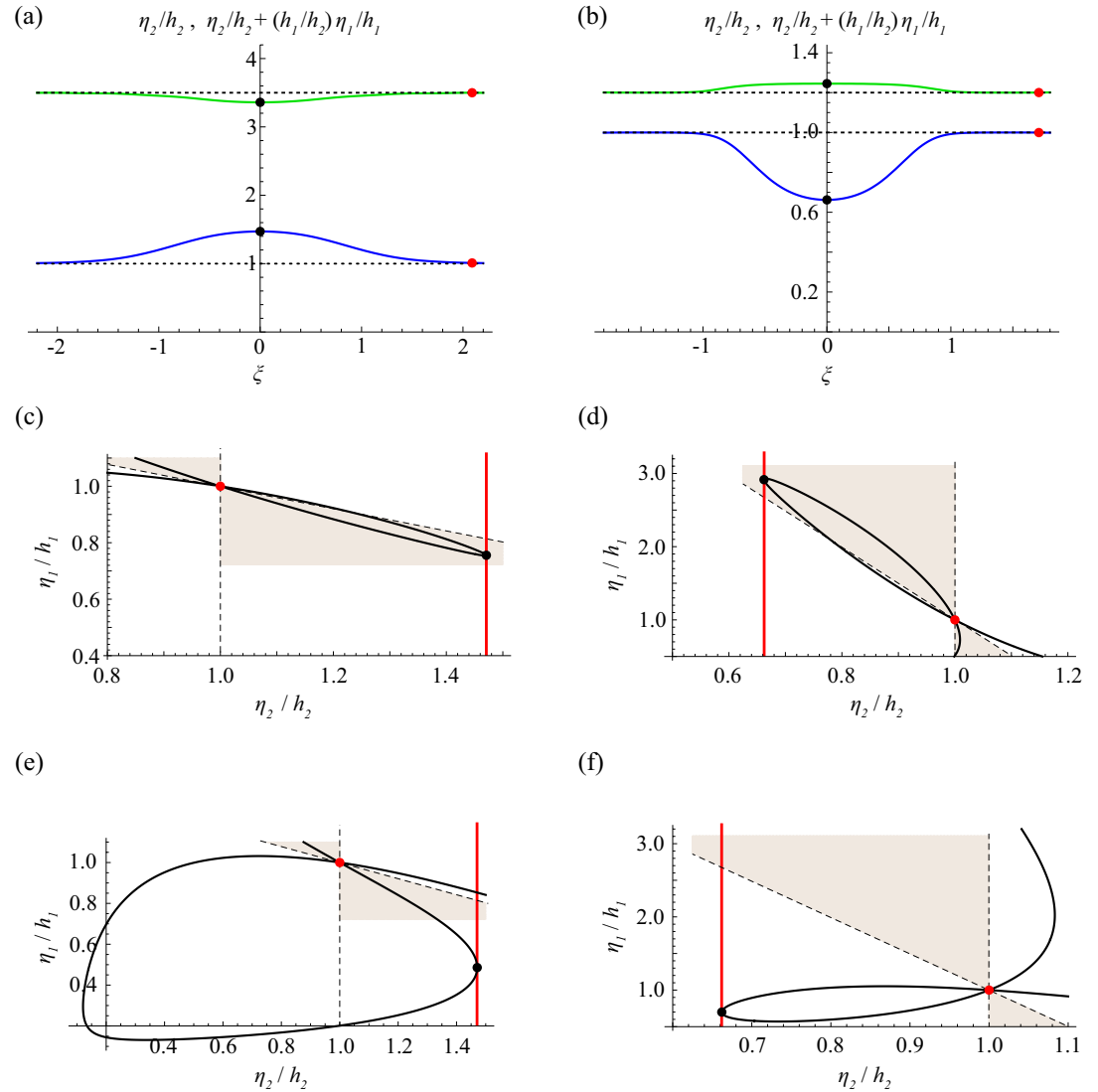


FIG. 3. Surface (green lines) and interfacial displacement (blue lines) for an ISWs of (a) elevation and (b) depression. The dimensionless abscissa  $\xi$  is linked to  $X$  as in Barros and Gavrilyuk<sup>39</sup>). The corresponding initial conditions portraits are obtained for (c,d) smallest and (e,f) largest celerity. Red dots refer to the undisturbed condition ( $\eta_1/h_1 = \eta_2/h_2 = 1$ ); black dots are associated to the maximum or minimum surface and interfacial displacements ( $\eta'_1(0) = \eta'_2(0) = 0$ ).

Froude number  $F = c/\sqrt{gh_2}$ , and computing the numerical integration of the differential system. We here propose a new technique valid for single-humped interfacial solitons, based on the same mathematical approach adopted for the *MCC-RL* and the *KdV* models. The authors are not able to provide a rigorous proof of the equivalence of this technique with the one proposed by Barros and

## The role of the free surface on interfacial solitary waves

Gavrilyuk<sup>39</sup> but its reliability is supported by lot of numerical tests. Basically, we assign as initial condition the ISW amplitude, namely at the point of minimum of the solitary wave interfacial profile at  $X = 0$  (the maximum is used in the case of ISW of elevation). Within the limits allowed by numerical precision, following our approach, the initial conditions are not in close proximity to the homoclinic orbit, but they exactly lie on it. To provide an heuristic explanation of this technique, we can primarily observe that the first derivatives of both the surface and the interfacial profiles are zero at  $X = 0$ , due to the wave symmetry. Here, the conserved quantity  $Ham$  solely depends on the layers thickness  $\eta_1(0)$  and  $\eta_2(0)$ . Moreover, the boundary condition at infinity (i.e.  $X \rightarrow \pm\infty$ ) requires  $\eta'_i \rightarrow 0$  and  $\eta_i \rightarrow h_i$ , so it results  $Ham = 0$  (see  $\beta_4$  in Appendix). Consequently, both the *critical point*  $(h_1, h_2)$  and  $(\eta_1(0), \eta_2(0))$  belong to the curve  $Ham = \beta_4 = 0$ . For the two examined cases, those special points are represented by red and black dots, respectively, in Fig. 3. The curve  $Ham = \beta_4 = 0$  is characterized by a loop shape very similar to an homoclinic orbit. However, it does not represent an orbit but has in common with it the aforementioned special points. We consider interfacial solitary waves of depression and elevation corresponding to the following set of dimensionless parameters:  $\rho_1/\rho_2 = 0.7$ ,  $h_1/h_2 = 0.2$ ,  $F = c/\sqrt{gh_2} = 0.3199$  and  $\rho_1/\rho_2 = 0.6$ ,  $h_1/h_2 = 2.5$ ,  $F = c/\sqrt{gh_2} = 0.6108$ ., respectively (see Fig. 3a,b). We plot the curve  $\beta_4 = 0$  in the plane of dimensionless variables  $\eta_i/h_i$ . The brown shaded area represents the zone where the limit amplitude conditions are fulfilled and the interfacial and surface waves are 180 degrees out of phase and (see Fig. 3c-f). All the numerical tests show that this condition is always fulfilled<sup>39</sup>. The special points have the maximum distance in the loop curve along the abscissa  $\eta_2/h_2$  since they represent the minimum and the maximum dimensionless displacements of both the free surface and the interface. Since the black point represent a *multiple root* of the equation  $\beta_4 = 0$  in the unknown  $\eta_1(0)/h_1$ , once the ISW amplitude is given, the corresponding elevation of the free surface can be obtained. Furthermore, the wave celerity  $c$  to use in the equation  $\beta_4 = 0$  has to assure *multiple root*. For this reason, the curve  $\beta_4 = 0$  is tangent to the red line, as in Figs. 3c-f. This condition leads to a fourth order biquadratic equation<sup>39</sup> in the unknown  $c^2$ , which admits two real solutions. After a large number of numerical tests, we observed that the lowest real solution always assures that the black point belong to the brown shaded region (as in Figs. 3c-d); otherwise, considering the largest celerity, the black point is always placed outside of it, and the corresponding numerical solutions of Eq. (13) shows a blow-up behavior, without physical meaning.

We implement our technique following two steps: (i) finding the limit amplitudes of the MCC-

The role of the free surface on interfacial solitary waves

*FS* model (the analogous of  $A_{RL}$  for the *MCC-RL* model); (ii) evaluating the celerity  $c$  and the amplitude of the free surface, assuming as input data  $\rho_1$ ,  $\rho_2$ ,  $h_1$ ,  $h_2$  and the amplitude of the interfacial wave. Then, substituting  $\eta_1 = h_1 - amp_1$ ,  $\eta_2 = h_2 + amp_2$  into  $\beta_4$ , with  $amp_1 \equiv (\zeta_2 - \zeta_1)$  and  $amp_2 \equiv \zeta_2$ , and solving the equation  $\beta_4 = 0$  with respect to  $c$ , the celerity for the *MCC-FS* model is obtained ( $c = c_{FS}$ ):

$$c_{FS} \equiv \pm \sqrt{\frac{g(h_1 - amp_1)(h_2 + amp_2)(amp_2^2 - 2amp_1amp_2\rho + amp_1^2\rho)}{amp_2^2(h_1 - amp_1) + amp_1^2\rho(h_2 + amp_2)}} \quad (15)$$

To obtain the limit value of the amplitudes  $Amp_1 = \zeta_{2max} - \zeta_{1max}$ ,  $Amp_2 = \zeta_{2max}$ , following the same approach used for the *MCC-RL* model, we look for the stationary points of the celerity  $c_{FS}$ , as a function of the amplitudes  $amp_1, amp_2$ , where  $\zeta_{1max}$  and  $\zeta_{2max}$  are the maximum surface and internal displacement, respectively. Assuming as constraints  $h_1 - Amp_1 > 0$ ,  $h_2 + Amp_2 > 0$ ,  $\zeta_{1max}\zeta_{2max} = Amp_2(Amp_2 - Amp_1) < 0$ , we solved numerically the following algebraic system of equations:

$$\begin{cases} \partial c_{FS} / \partial amp_1 = 0 \\ \partial c_{FS} / \partial amp_2 = 0 \end{cases} \quad (16)$$

Only one solution ( $Amp_1, Amp_2$ ) has been found in many numerical tests satisfying both system (16) and the adopted constraints. These means that the local thicknesses must be positive and to an up (down) interfacial wave displacement a down (up) surface wave displacement is associated. Coming back to the previous problem of initial conditions of the differential system (13), the four values of  $\eta_i(0)$  and  $\eta'_i(0)$  ( $i = 1, 2$ ) have to be assigned. If the minimum or maximum of wave profile are in  $X = 0$ , it follows  $\eta'_i(0) = 0$ . The displacements  $amp_1, amp_2$  have to fulfill the limitations  $|amp_i| \leq |Amp_i|$ . However, those conditions together with  $amp_2(amp_2 - amp_1) < 0$  are necessary but not sufficient to integrate the differential system (13). Many numerical tests show that integration of the *MCC-FS* model highlights solutions with a rapid blow-up behavior without physical meaning, namely these solutions are not *homoclinic orbits*. Only when a very accurate match between  $amp_1$  and  $amp_2$  is fulfilled, then the numerical solutions exhibit a soliton profile. One interesting question is, once assigned the separation surface displacement  $\zeta_2 = amp_2$ , which value of the free surface displacement  $\zeta_1 = amp_2 - amp_1$  can assure a soliton solution of the differential system (13). To address this issue, we performed a large number of numerical tests, and with a similar approach used for the *KdV* and the *MCC-RL* models, we found that  $amp_1$  must satisfy a polynomial equation with *multiple roots*. However, differently from the other model, for

The role of the free surface on interfacial solitary waves

the *MCC-FS* model this condition *has to be imposed*.

As already observed  $(c_{FS}, amp_1, amp_2)$  satisfy the equation  $\beta_4 = 0$  which can be written as a cubic equation in the unknown  $amp_1$ :

$$amp_1^3 + b_1 amp_1^2 + b_2 amp_1 + b_3 = 0 \quad (17)$$

with:

$$\begin{cases} b_1 \equiv (\frac{c_{FS}^2}{g} - 2amp_2 - h_1) \\ b_2 \equiv amp_2(2h_1 + \frac{amp_2(g(amp_2+h_2)-c_{FS}^2)}{g(amp_2+h_2)\rho}) \\ b_3 \equiv \frac{amp_2^2 h_1 (c_{FS}^2 - g(amp_2+h_2))}{g(amp_2+h_2)\rho} \end{cases} \quad (18)$$

To assure real and *multiple roots*, the discriminant  $\Delta$  of the cubic (17) must be zero. For a cubic equation, as well known,  $\Delta = Q^3 + R^2$  where  $Q \equiv (1/9)(3b_2 - b_1^2)$  and  $R \equiv (1/54)(9b_1b_2 - 27b_3 - 2b_1^3)$ . Assigning  $amp_2, (|amp_2| \leq |Amp_2|)$  the equation  $\Delta = \Delta(amp_2, c_{FS}) = 0$  can be numerically solved with respect to  $c_{FS}$ , by choosing the lowest positive real solution. Finally, solving the cubic equation (17), the value of  $amp_1$  is obtained, choosing the multiple root.

In conclusion, to integrate numerically system (13), assigned the value of the separation surface displacement  $amp_2 : |amp_2| \leq |Amp_2|$ , with the previous algorithm, it is possible to calculate univocally  $c_{FS}$  and  $amp_1$ . Thus, the initial conditions at the point  $X = 0$  of maximum or minimum in order to obtain soliton solutions are:

$$\begin{cases} \eta_1(0) = h_1 - amp_1 \\ \eta_2(0) = h_2 + amp_2 \\ \eta_1'(0) = 0 \\ \eta_2'(0) = 0 \end{cases} \quad (19)$$

For all the performed numerical tests,  $\zeta_2 = amp_2$  and  $\zeta_1 = amp_2 - amp_1$  have opposite sign, namely to an up (down) interfacial wave profile corresponds a down (up) free-surface wave profile.

#### D. Theoretical ISW features

The ISWs size and the ambient fluid stratification affect the waves profile. We analyze theoretical ISWs propagating into two stratified systems with fixed layers thickness (i.e.,  $h_1/h_2 = 0.2$ ),

# The role of the free surface on interfacial solitary waves

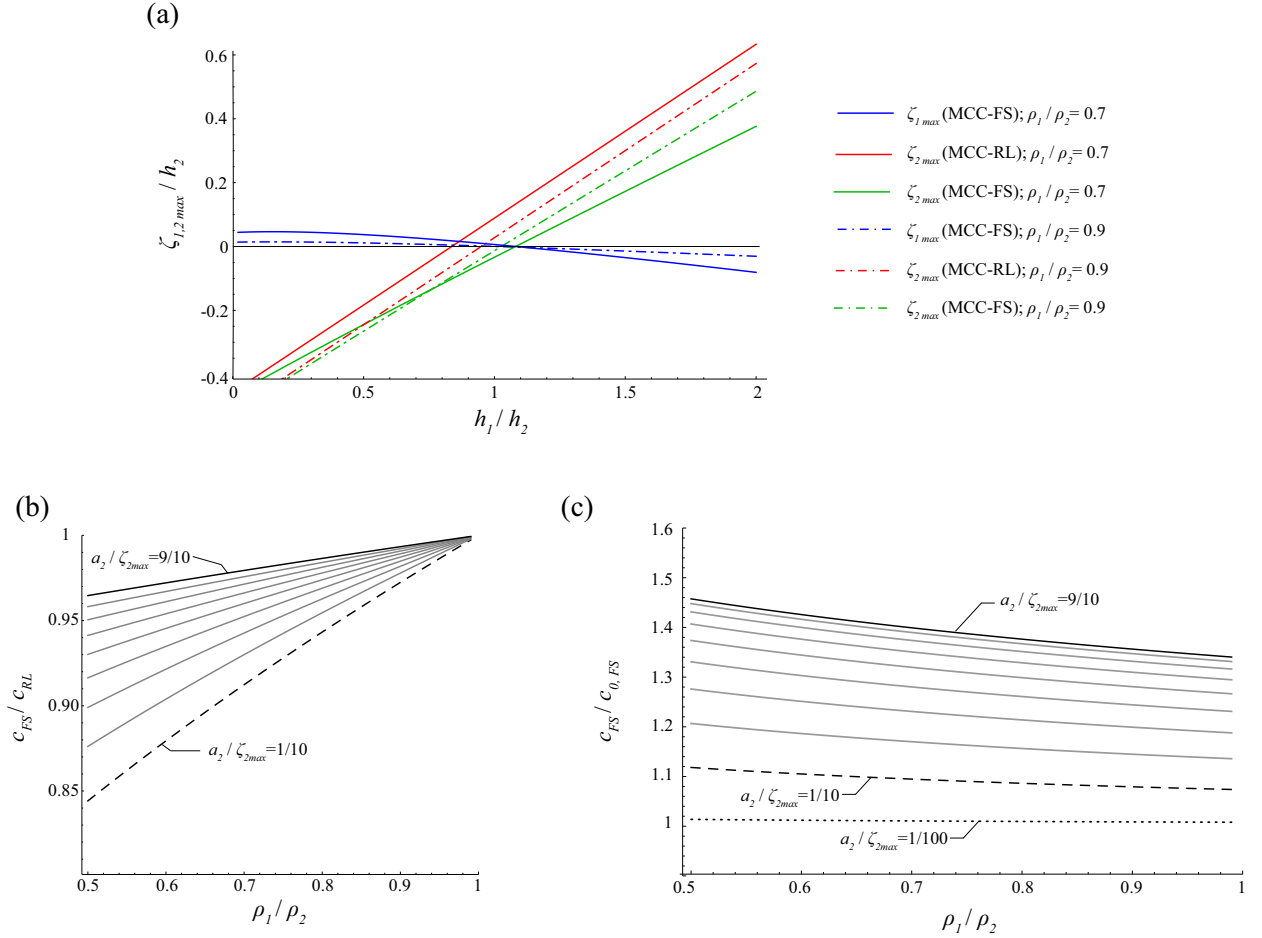


FIG. 4. (a) Relation between the dimensionless upper layer thickness  $h_1/h_2$  and the dimensionless maximum displacement of both the interface  $\zeta_{2max}/h_2$  and the surface  $\zeta_{1max}/h_2$ , for density ratios  $\rho = 0.7$  and  $0.9$ . (b) Relation, for different ISWs amplitudes (i.e. for  $0.1 < a_2/\zeta_{2max} < 0.9$ , with step  $0.1$ ) between  $\rho$  and the ratio of ISWs celerities predicted by the *MCC-FS* and by the *MCC-RL* models. (c) Relation, for different ISWs amplitudes (i.e. for  $0.1 < a_2/\zeta_{2max} < 0.9$ , with step  $0.1$ ) between  $\rho$  and the ISWs celerities predicted by the *MCC-FS* model normalized by the linear long-wave speed  $c_{0,FS}$ . The *MCC-FS* celerity approaches the linear long-wave speed as  $a_2/\zeta_{2max}$  tends to  $0$  (e.g. see the dashed line for  $a_2/\zeta_{2max} = 0.01$ ).

but different density ratios (Fig. 2). In particular, both Boussinesq ( $\rho = 0.9$ ) and non-Boussinesq ( $\rho = 0.6$ ) flow conditions are set up<sup>40</sup>. Although the *KdV* model does not provide mathematical limits for the the interfacial amplitude, the predicted wave profiles are consistent with our experimental observations only for  $a_2/h_1 < 0.4$ , i.e. for small amplitude solitary waves<sup>18</sup>. We thus investigate models results for both large and small amplitude ISWs (i.e.,  $a_2/h_1 \approx 1$  in Fig. 2a,c and  $a_2/h_1 \approx 0.1$  in Fig. 2b,d, respectively).



# The role of the free surface on interfacial solitary waves

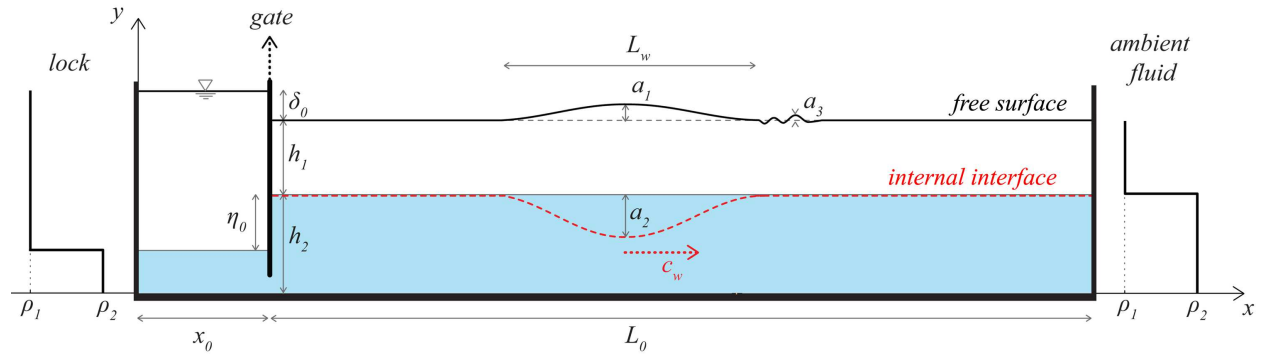


FIG. 5. Schematic view of the experimental set up and density distributions within the Perspex flume. Internal solitary waves are generated in a stratified fluid system composed by Vaseline oil and a saline mixture of sodium chloride, with density  $\rho_1 = 856.0 \text{ kg/m}^3$  and  $\rho_2 > \rho_1$ , respectively. The vertical gate, separates two regions having different density distributions: the lock on the left ( $x_0 = 0.3$  long) and the ambient fluid on the right ( $L_0 = 2.695$  m long). Before the gate removal the initial interfacial displacement  $\eta_0$  and the free surfaces displacement  $\delta_0$  are produced. Lifting up the gate, the generation of an internal solitary wave of depression occurs, characterized by an amplitude  $a_2$ , a wavelength  $L_w$  and a celerity  $c_w$  (red dashed line). Associated with it, a surface soliton with the same celerity and wavelength propagates downstream with amplitude  $a_1$  (black solid line). It is foregone by a train of 2-3 relatively smaller surface waves whose larger has an amplitude  $a_3$ .

The almost overlapped wave profiles obtained for small amplitude ISWs propagating in a smoothly stratified ambient fluid, confirm the reliability of the obtained results (Fig. 2d). Moreover, the top free surface boundary condition does not considerably affect results, which are in accordance with those obtained by mathematical models with a rigid lid approximation. This is also observed for large amplitude conditions for cases with density ratio closer to 1 (Fig. 2c). The wave profiles predicted by the strongly nonlinear *MCC* models are clearly broader than those resulting from the *KdV* theory, which is unreliable for considerably large amplitudes waves.

Non-Boussinesq flow conditions enhance, instead, surface manifestations, also for small amplitude ISWs. For both *KdV* and *MCC* models, the resulting wave profiles result narrower than those obtained with rigid lid boundary conditions (see dashed lines in Fig. 2b). The four interfacial displacements significantly diverge for large amplitude ISWs propagating into strongly stratified fluids (Fig. 2a). Under those conditions, both the free surface and the strong nonlinearity affect the models predictions, whose reliability needs to be tested by comparing theoretical results and

## The role of the free surface on interfacial solitary waves

experimental observations, as discussed herein (Section IV).

Contrary to the *KdV* theory, the *MCC* models admit upper limit amplitudes for both top free surface and rigid lid conditions ( $\zeta_{2max}(MCC-RL)$ ) and  $\zeta_{2max}(MCC-FS)$ ). Associated to  $\zeta_{2max}(MCC-FS)$ , the corresponding upper limit for the free surface displacement is  $\zeta_{1max}(MCC-FS)$ . We study how those limit values change depending on the stratification features, i.e., for different layers density and thickness. The investigated density ratios are  $\rho=0.7$  and  $\rho=0.9$  (solid and dashed lines, respectively, in Fig. 4a). Approximately for  $h_1/h_2 < 1$  the resulting ISW has a facing upward concavity. The associated maximum interfacial and surface amplitudes assume negative and positive values, respectively. An opposite behavior occurs for  $h_1/h_2 > 1$ , approximately<sup>39</sup>.

The analysis of the limiting interfacial and surface amplitudes reveal some interesting features of solitary waves with a very large amplitude. For  $0.5 < h_1/h_2 < 1.5$ , the absolute value of the free surface displacement  $\zeta_{1max}$  predicted by the *MCC-FS* model is almost linearly related with  $h_1/h_2$  (see solid and dashed blue line in Fig. 4a). This means that larger surface manifestations are expected for ISWs of depression propagating in a stratified ambient fluid with a thinner upper layer, or a stronger stratification. Otherwise, for ISWs of elevation, the same behavior occurs increasing the normalized upper layer thickness. Decreasing  $h_1/h_2$  from 0.5 to 0, instead, the dimensionless surface displacement remains roughly unvaried, although the interfacial amplitude increases. For ISWs of depression, the convergence of  $\zeta_{2max}(MCC-FS)$  and  $\zeta_{2max}(MCC-RL)$  can be clearly observed for decreasing upper layer thicknesses. Those results suggest that the effect of the free surface on the overall flow field fades for interfacial profiles with larger amplitudes. The opposite behavior occurs for ISWs of elevation: increasing  $h_1/h_2$  from 1.5 to 2, the divergence of  $\zeta_{2max}(MCC-FS)$  and  $\zeta_{2max}(MCC-RL)$ , and the continuous increase of the surface displacement are observed. For ISWs of elevation, the presence of a top free surface affects more and more the flow features as the undisturbed internal interface is located at a larger depth.

To deeply investigate how the flow is affected by the free surface, we introduce the ratio between the celerities predicted by the *MCC* model for different boundary conditions:  $c_{FS}/c_{RL}$ . The more those celerities differ the more the free surface affects the ISWs features. This occurrence is observed both for increasing density difference and solitary waves with lower amplitudes (e.g., see solid black line in Fig. 4b). For a possible physical explanation of this behavior one should consider that ISWs grow in size deepening, namely increasing their interfacial amplitude more than the surface displacement (Fig. 4a). Moreover, the rigid lid condition ensures always a larger ISW celerity because the flow is unable to transfer part of its energy in producing surface manifesta-

The role of the free surface on interfacial solitary waves

tions (Fig. 4a). Thus, for larger waves, a lower amount of the wave energy is transferred at the free surface, and the wave celerity is closer to that resulting from a rigid lid approximation.

For different dimensionless interfacial amplitudes, Fig. 4c shows the ratio between the celerity predicted by the *MCC-FS* model and the linear-long-wave-celerity of the linearized *MCC-FS* model<sup>33</sup>, defined as:

$$c_{0,FS} = \sqrt{\frac{1}{2}g \left( h_1 + h_2 - \sqrt{4h_1h_2\rho + (h_1 - h_2)^2} \right)}. \quad (20)$$

The celerity ratio grows with the dimensionless wave amplitude, since the celerity predicted by the *MCC-FS* model assumes even more larger values with respect to the linear-long-wave-celerity. For large amplitude ISWs, the relative growth rate of wave celerity with the dimensionless amplitude becomes increasingly slower (Fig. 4c).

### III. LABORATORY EXPERIMENTS

#### A. Experimental procedure

We performed a series of 13 laboratory experiments at the Hydraulics Laboratory of Roma Tre University in a 3.0-m-long, 0.2-m-wide, and 0.3-m-deep Perspex tank (Fig. 5).

An immiscible two-fluid system is set up following the standard lock-release method<sup>30</sup>. Following the same experimental procedure used by<sup>32</sup>, the tank is first filled with a uniform saline mixture of sodium chloride (NaCl) of density  $\rho_2$ . In order to visually distinguish the two layers and the interface position, we add a controlled amount of methylene blue to dye the saline mixture. Later, Vaseline mineral oil (ENOL SPRINT B/50) is slowly poured on the free surface composing a second lighter layer of uniform density  $\rho_1 = 856.0 \text{ kg/m}^3$  and thickness  $h_1$ . A 5 mm thick, Perspex gate is then vertically inserted at  $x_0 = 0.3 \text{ m}$  from the left wall of the flume, dividing the tank into two regions: the lock on the left and the ambient fluid on the right. The gate does not touch the channel bottom, preserving the hydraulic continuity between the two parts. Thus, adding Vaseline oil on the free surface of the lock region, a known amount of brine water flows into the ambient fluid, creating the displacement  $\eta_0$  between the internal interfaces (Fig. 5). Reached the hydrostatic balance, the lower layer in the ambient fluid reaches a thickness  $h_2$ , and a displacement  $\delta_0$  forms between the free surfaces divided by the lock gate.

## The role of the free surface on interfacial solitary waves

Each experiment begins as the gate is manually removed. We take care to not completely lift the gate away from the free surface, but just below it. The goal of this adjustment is to minimize the disturb that a complete gate removal would induce. After the collapsing mechanism produced by the initial interfacial displacement  $\eta_0$ , the generation of an internal solitary wave of depression occurs. It propagates downstream preserving its celerity  $c_w$  and shape, i.e. amplitude  $a_2$  and wavelength  $L_w$  (see dashed red lines in Fig. 5). Due to the large density difference characterizing the stratification, also surface manifestations are observed. A surface solitary-like wave follows the internal displacement such that they propagate with the same celerity and wavelength, but the first with lower amplitude ( $a_1 < a_2$  in Fig. 5). Ahead of the leading edge of the surface displacement, also a train of small-amplitude, short, periodic waves are observed propagating with the same internal displacement celerity. For each experiment, we characterize those waves by evaluating the larger amplitude value they assume during motion ( $a_3$  in Fig. 5). As the group of internal and surface manifestations reaches the right-hand side of the tank, a reflection process occurs. Each experiment is considered finished as the leading edge of the reflected ISWs flows back again to the gate. For all the performed cases, we observe that incident and reflected ISWs features slightly change: a decrease of the ISWs amplitude and wavelength and an increase of their celerity occurs. To associate an overall value of amplitude, wavelength and celerity to each incident and reflected ISW, we evaluate their main features as they pass the cross section placed  $L_0/2$  away from the gate. We checked, indeed, that the transient effects induced by the gate removal or by the reflection process vanishes at this location, i.e. each ISW reaches a steady state.

We remark that the effect of the lateral walls of the tank can be considered negligible, as shown in previous experimental studies<sup>15,41</sup>.

We obtain results from 13 laboratory experiments characterized by different initial conditions (see Tab. I), to analyze how the initial setting parameters affected the flow features. For each case, we evaluate the main wave features and the associated surface manifestations. We investigate the effect of  $\delta_0$  on the fluid dynamics, for three experiments, i.e. cases 3, 4 and 5. For those cases, characterized by different ratios  $\eta_0/h_1$ , we set the free surfaces separated by the gate at the same level. The gate is completely inserted, up to the flume bottom. Then, the light fluid within the lock is gradually removed until all the fluid present in the tank reaches the same total level. For all the other cases, the gate is inserted ensuring the hydraulic continuity between the fluids it separates. We performed 7 experiments with increasing ratios  $\eta_0/h_1$ , to widen the range investigated by Kodaira *et al.*<sup>33</sup>, and to evaluate the effect of very thin surface layers. Cases 9 and

The role of the free surface on interfacial solitary waves

10 present values of  $h_1$  one order of magnitude lower with respect to the other experiments. A crucial parameter affecting the flow features is the density ratio  $\rho$  characterizing the stratification. The adopted combinations of fluids have density ratios always lower than those used by Kodaira *et al.*<sup>33</sup> (i.e. 0.85). In particular, for most of the experiments we used  $\rho = 0.80 \div 0.81$ , while  $\rho = 0.72$  is set for three cases (i.e. 11, 12 and 13), a value in close proximity to non-Boussinesq flow conditions. The Reynolds number is evaluated as<sup>42</sup>:

$$Re_w = \frac{a_2 C_0}{\nu} \quad (21)$$

where  $C_0 = (g'h_1h_2/H)^{0.5}$  is the linear wave phase speed, and  $g' = g(\rho^{-1} - 1)$  is the reduced gravity. The kinematic viscosity  $\nu$  is obtained as the mean kinematic viscosity weighted on the layers thickness. Due to a larger kinematic viscosity, we obtain Reynolds numbers (i.e.  $0.92 \times 10^3 \div 4.70 \times 10^3$ ) with the same order of magnitude of those observed in previous experiments, for which considerably lower density gradients have been used<sup>15</sup>.

## B. Measurements techniques and errors

A density meter (Anton Paar DMA 4100M) was used to measure the density of both the saline mixture and the Vaseline oil. Its measurement accuracy was  $0.1 \text{ kg/m}^3$ . Based on the material safety data sheet, the kinematic viscosity of the Vaseline oil is  $\nu_0 = 4 \times 10^{-5} \text{ m}^2/\text{s}$ .

The saline mixture was prepared within the tank where a known amount of salty was properly dissolved in fresh water. We checked that the concentration was uniform by measuring density along the tank and at different depths. Accuracy of density and length measurements was assessed by verifying that the measured free surfaces displacements were close enough to the theoretical value, obtained by the hydrostatic balance (Fig. 6)

$$\delta_0 = \eta_0 \frac{\rho_2 - \rho_1}{\rho_1} = \eta_0 \left( \frac{1}{\rho} - 1 \right) \quad (22)$$

where  $\rho = \rho_1/\rho_2$  is density ratio characterizing the stratification. Once the initial setting of each experiment was properly obtained we measured the actual layers thickness by using a ruler, with an accuracy of 1 mm.

At a fixed distance from the front wall of the tank, a digital camera (Sony RX100 IV) with a frequency of 50 Hz and a spatial resolution of  $1920 \times 1080$  pixels was placed to record the flow

## The role of the free surface on interfacial solitary waves

TABLE I. Initial setting parameters (i.e., the density ratio  $\rho = \rho_1/\rho_2$ , the free surface displacement  $\delta_0$ , the initial interfacial displacement  $\eta_0$ , and the upper and lower layer thicknesses within the ambient fluid  $h_{1,2}$ ), and main flow features (i.e. the surface solitary wave amplitude  $a_1$ , the interfacial maximum displacement  $a_2$ , characteristic wavelength  $\lambda_2$  and celerity  $c_w$ ). Asterisks are used in superscripts to indicate the same parameters described above after the ISWs was reflected from the right-end side of the flume.

Case	initial setting			incident phase						post-reflection phase					
	$\rho$	$\delta_0$	$\eta_0$	$h_1$	$h_2$	$a_1$	$a_2$	$\lambda_2$	$c_w$	$h_1^*$	$h_2^*$	$a_1^*$	$a_2^*$	$\lambda_2^*$	$c_w^*$
	-	cm	cm	cm	cm	cm	cm	cm	cm/s	cm	cm	cm	cm	cm	cm/s
1	0.81	1.1	4.5	3.3	24.0	0.4	2.2	29.7	30.2	3.5	23.9	0.3	1.6	29.7	28.7
2	0.81	1.9	8.1	3.2	22.1	0.5	4.3	37.8	34.2	3.8	21.7	0.5	3.0	35.1	32.9
3	0.80	0.0	7.2	4.0	22.2	0.3	2.8	37.8	33.2	4.3	21.9	0.3	2.2	29.7	31.2
4	0.80	0.0	12.2	3.2	23.0	0.4	4.9	40.5	34.2	3.8	22.4	0.4	3.4	35.1	31.7
5	0.80	0.0	18.2	2.6	23.7	0.5	7.2	40.5	34.8	3.8	22.5	0.5	5.2	35.1	34.2
6	0.80	1.7	6.8	4.0	22.2	0.4	3.3	40.5	33.2	4.3	22.1	0.4	2.7	37.8	31.7
7	0.80	3.0	12.3	3.4	22.8	0.7	6.0	45.9	35.8	4.1	22.4	0.5	4.8	40.5	34.2
8	0.80	4.7	18.8	2.6	23.5	1.0	8.6	51.3	37.9	3.8	22.8	0.6	6.7	45.9	35.9
9	0.81	3.7	14.8	0.9	26.4	0.8	7.7	35.1	36.0	2.3	25.4	0.6	4.2	29.7	31.2
10	0.81	3.9	17	0.5	26.6	0.9	8.4	40.5	39.0	2.1	25.4	0.6	4.6	32.4	30.4
11	0.72	3.2	7.8	4.1	22.0	0.8	4.3	48.6	41.9	4.6	21.8	0.7	3.4	43.2	41.7
12	0.72	5.1	12.2	3.6	22.3	1.1	6.4	54.0	44.0	4.3	22.1	0.9	5.5	45.9	42.9
13	0.72	6.8	16.7	2.9	22.8	1.3	8.0	59.4	43.7	4.2	22.2	1.0	6.7	48.6	44.2

evolution. Each pixel had a resolution of about  $1.7 \times 1.7 \text{ mm}^2$ . Using image analysis, the instantaneous interface and free surface positions were inferred (see blue and yellow lines in Fig. 7a). We then obtained some geometric and kinematic features of the ISWs, such as the wave amplitude  $a_2$ , the wave celerity  $c_w$ , as well as the maximum surface displacement  $a_1$  (Fig. 5). We obtained the ISW celerity as the first derivative of the trough's position (see point C Fig. 7a). The error committed for lengths measurements is about 1 pixel. Taking into account the camera acquisition frequency and the pixel size, the celerity was affected by an averaged relative error of 2%. To estimate the length of the leading internal waves, we evaluated firstly the wavelength  $L_w$  as the horizontal distance between the wave ends (see Fig. 5). In presence of secondary waves, the



## The role of the free surface on interfacial solitary waves

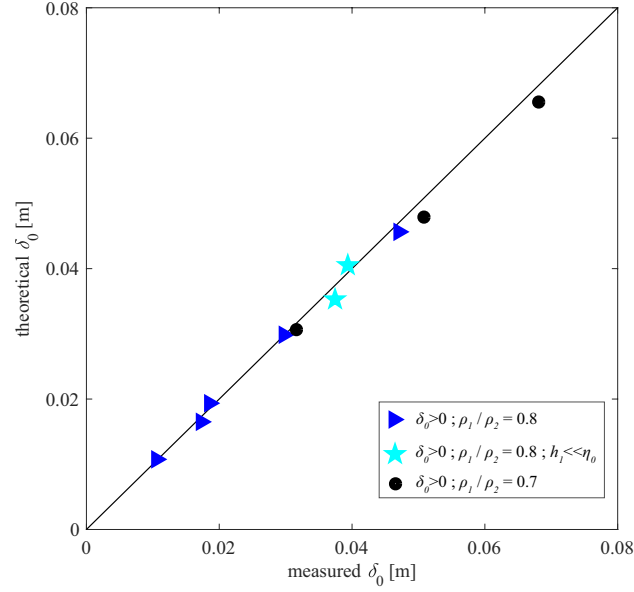


FIG. 6. Comparison between the measured free surface displacements and the expected values obtained by hydrostatic equilibrium. Each mark refer to a defined initial setting condition, defined in the figure legend.

leading wave was confined upstream by the lowest point of the internal interface between the two crests (see points *A* and *B* in Fig. 7a). We then estimated the ISW characteristic wavelength, obtained as in<sup>31</sup> by the following relation:

$$\lambda_w = \frac{1}{a_2} \int_{-\infty}^{+\infty} \eta(x) dx \simeq \frac{1}{a_2} \int_A^B \eta(x) dx = \frac{S_w}{a_2} \quad (23)$$

where  $\eta(x)$  is the interfacial vertical displacement compared to its original position, and  $S_w$  is the ISW surface. The latter was evaluated as the area subtended by the displaced internal interface with respect to its original position.

### C. Flow features

The fluids divided by the lock gate interact as the watertight vertical gate is lifted up. Because of their different density profiles, the light layer confined into the lock immediately slumps upward into the shallower light water ambient, launching a train of hump-shaped internal solitary waves of depression, which propagate downstream (Fig. 7a). The internal wave packet is composed by gradually smaller (i.e. slower) ISWs. The gray-scale field obtained for case 11 in the horizontal plane  $(x, t)$  at a fixed depth ( $y = 21$  cm), shows the wave packet transition (Fig. 7b). Among all

# The role of the free surface on interfacial solitary waves

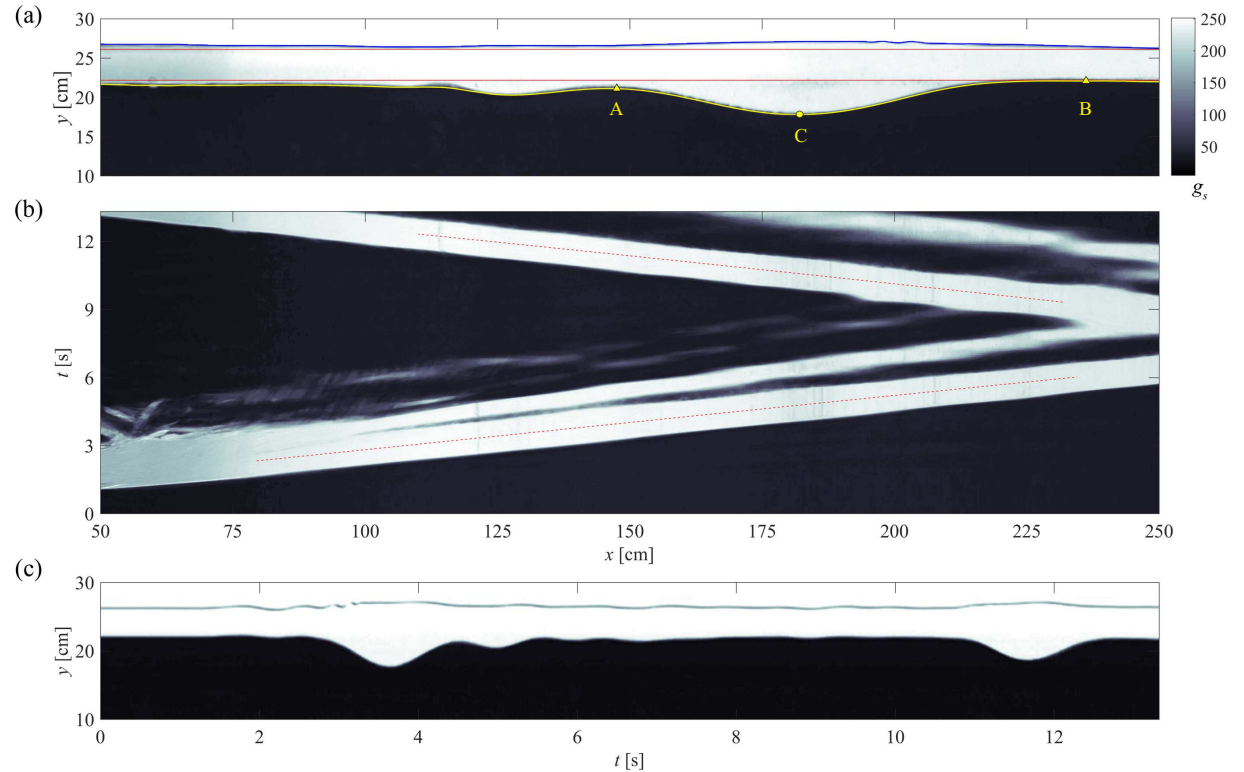


FIG. 7. Case 11: (a) Snapshot of the flow field captured 4.78 s after the gate removal; (b) gray-scale field in the horizontal plane  $(x, t)$  situated at a fixed depth  $(y = 21 \text{ cm})$ ; (c) gray-scale field in the vertical plane  $(t, y)$  at 1.05 m away from the lock gate. By image analysis we obtained the instantaneous position of both the free surface (solid blue line) and the internal interface (solid yellow line); the solid red lines indicate their positions at the begin of the experiment. We inferred the instantaneous location of the internal wave trough (point C and red dotted lines). The solid red lines indicate the free surface and the interface positions at the begin of the experiment. Points A and B are the internal wave upstream and downstream boundaries, respectively.

the performed experiments, Case 11 is chosen as representative in order to describe some common flow features observed for the other cases. Each internal wave propagates with approximately constant celerity  $c_w$  depending on both the wave geometric features and the stratification structure. Being the wave packet composed by ordered in size ISWs, their mutual distance gradually increases during motion (see the different slopes of the light bands in (Fig. 7b) for  $t < 7 \text{ s}$ ). The leading wave thus separates from the following ones. The internal wave packet reaches the right-end side of the tank where ISWs are reflected (Fig. 7b) for  $t > 7 \text{ s}$ ). Reflection process induces a

## The role of the free surface on interfacial solitary waves

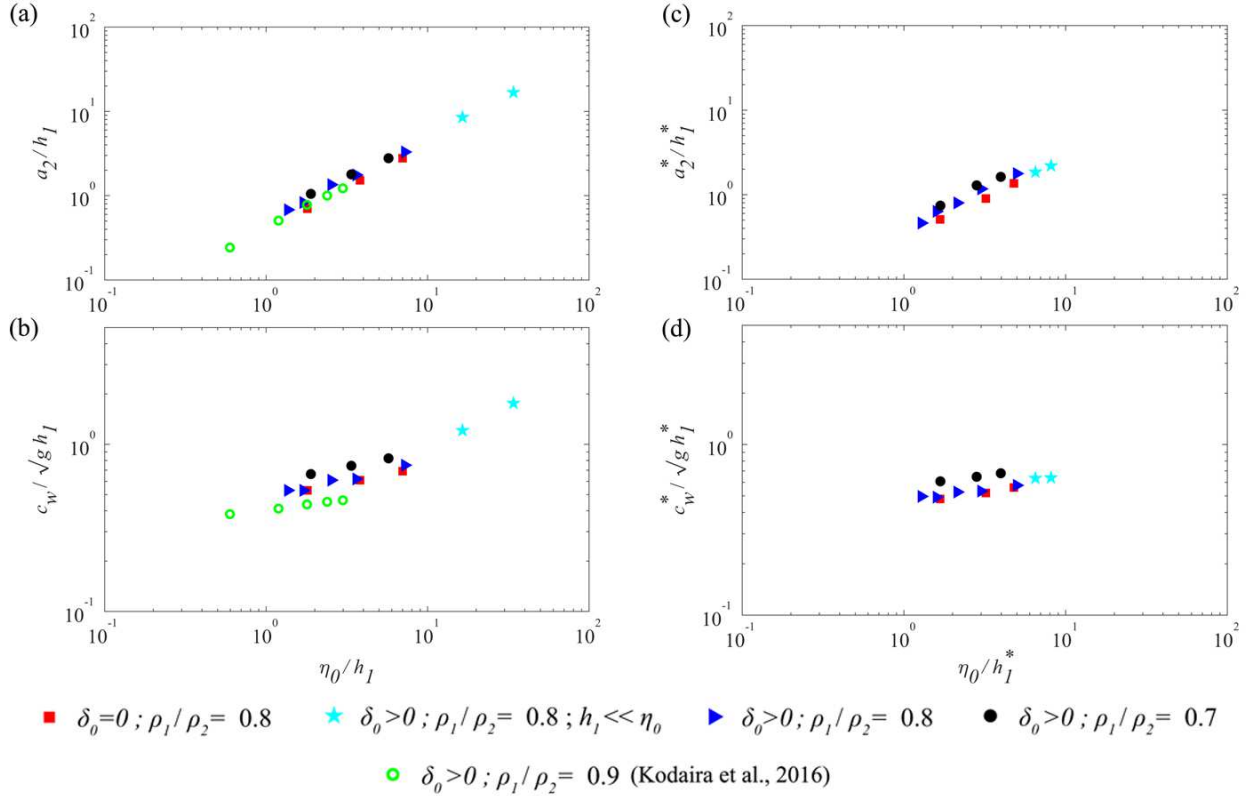


FIG. 8. Comparison between the the initial interface displacement  $\eta_0$  and the resulting ISW amplitudes  $a_2$  (a,c) and celerities  $c_w$  (b,d). Both ISWs amplitudes and interface displacements are non-dimensionalized by using the top layer thickness  $h_1$ , while ISW celerity is normalized by  $\sqrt{gh_1}$ . Parameters with asterisk in superscript refer to reflected ISWs (c,d). Experimental data are shown in logarithmic scales for both the x- and the y-axis. Each mark is associated to a defined initial setting condition, defined in the figure legend.

partial dissipation of the internal waves causing a decrease of their main features (i.e. amplitude, wavelength and celerity).

By image analysis, we estimate the instantaneous interface and surface profiles (yellow and blue lines in Fig. 7a, respectively). This allows us to identify the internal wave trough (point C) and the wave horizontal extent. The leading edge of the internal wave starts from point B where the interface profile departs from its undisturbed position (lower red line). For all the performed experiments, the ISWs present a slight asymmetry with respect to the trough position. The trailing edge of the wave is confined by point A, located deeper with respect to point B. This occurrence seems to be not related to the presence of the following waves, since it was observed also at later stages, when the leading wave separates from the following one, as well as after its reflection.

# The role of the free surface on interfacial solitary waves

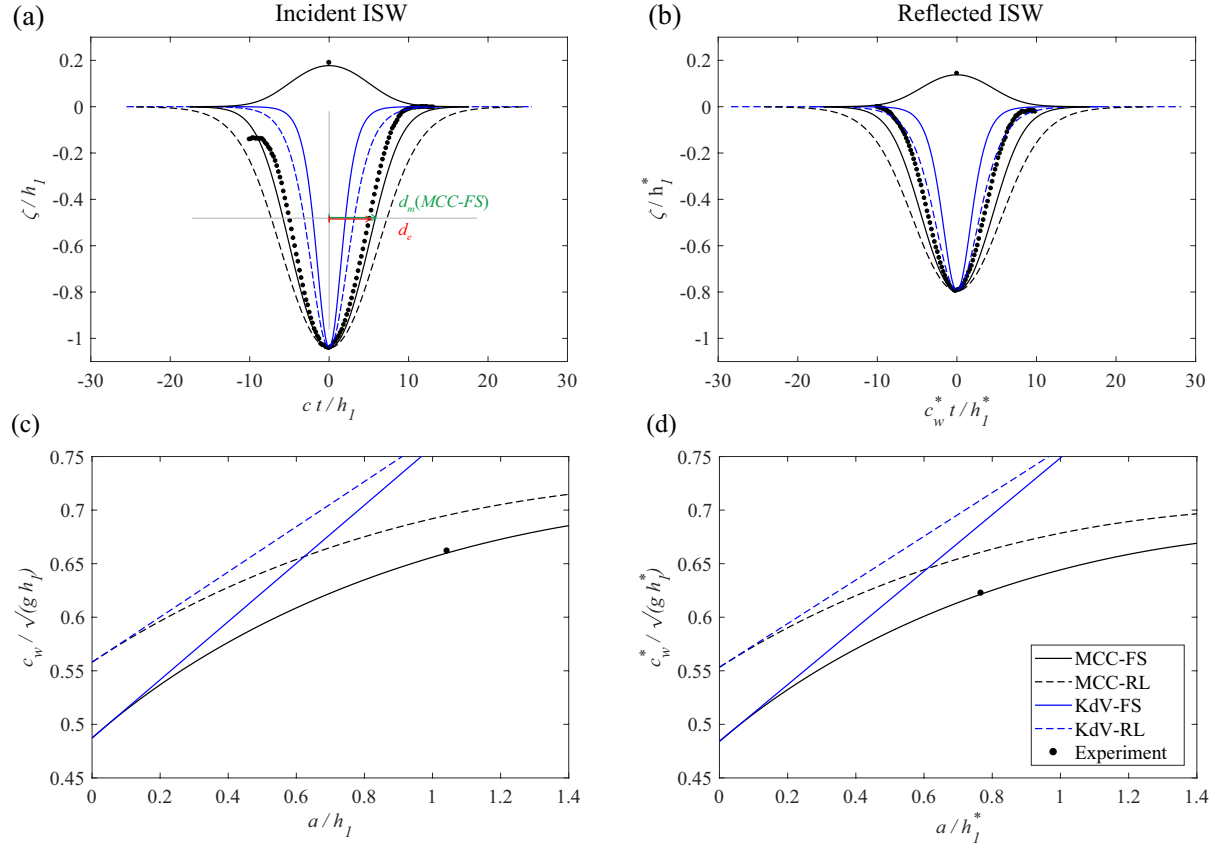


FIG. 9. Experimental (dots) and theoretical (lines) wave profiles for (a) incident and (b) reflected ISW (Case 11). The free surface maximum displacement inferred from Case 11 is shown and compared with the surface profile predicted by the *MCC-FS* model. The profiles are normalized by using the top layer thickness  $h_1$ . Measured celerity  $c_w$  versus amplitude  $a_2$ , non-dimensionalized by  $\sqrt{gh_1}$  and  $h_1$  respectively, for (c) incident and (d) reflected ISW (Case 11). Dots, experimental data; black line, *MCC-FS*; black dashed line, *MCC-RL*; blue line, *KdV-FS*; blue dashed line, *KdV-RL*. Red and green arrows refer to the horizontal distances, measured along the wave mid-depth, from the wave crest to the experimental and theoretical profile, i.e.  $d_e$  and  $d_m(MCC-FS)$ , respectively.

More properly, the wave profiles asymmetry could be caused by the shear across the interface, which is expected to increase with both ISWs amplitude and density difference between the two layers<sup>18</sup>. We observed shear stress instabilities mainly develop on the ISWs trailing edge, causing discontinuities of the wave profile. The same behavior was observed by Kodaira *et al.*<sup>33</sup>, who suggested that the surface tension between the two immiscible fluids opposed the shear-induced overturning, thus avoiding the generation of Kelvin Helmholtz billows.

After reflection, ISWs partially dissipate: a decrease of the wave geometric and kinematic features

# The role of the free surface on interfacial solitary waves

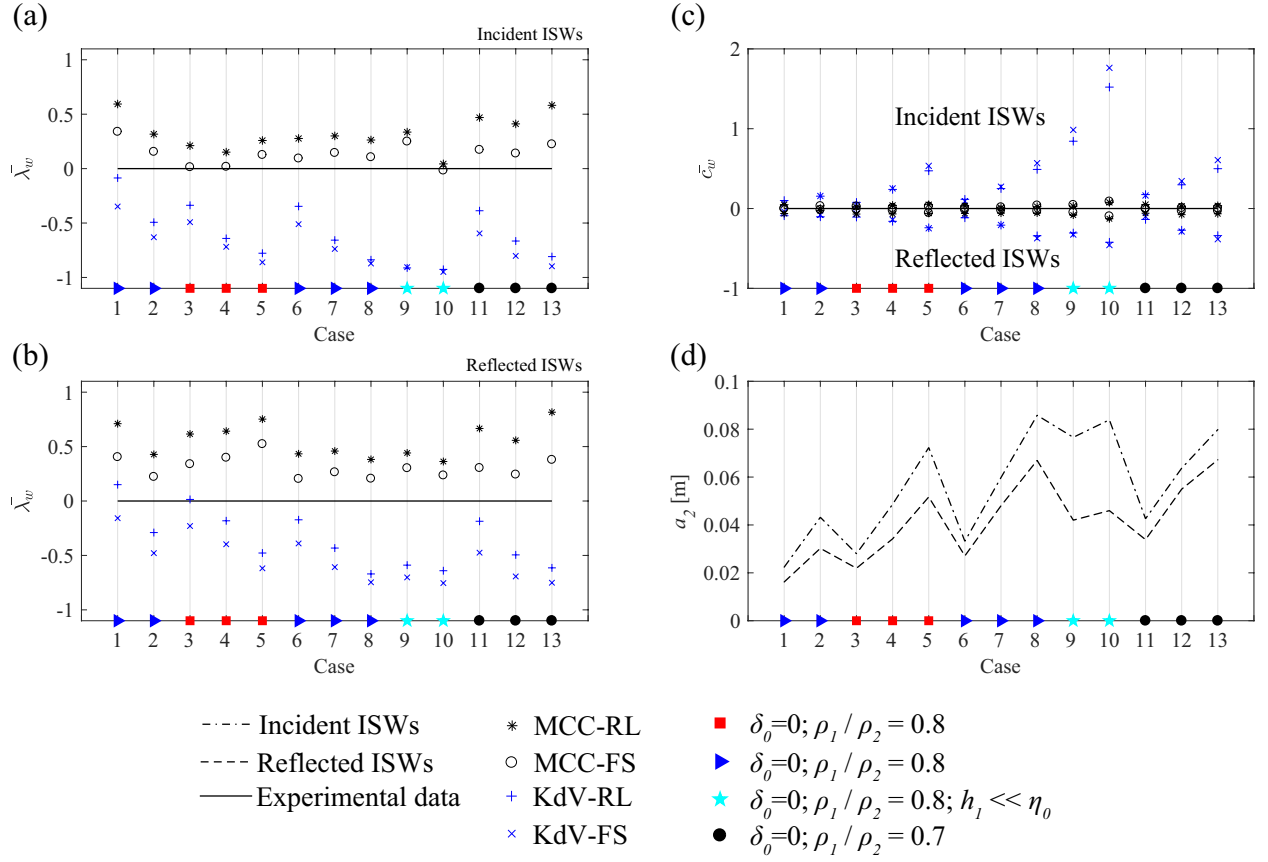


FIG. 10. The experimental and theoretical wave profiles are compared in terms of normalized difference at the wave the mid-depth  $\bar{\lambda}_m$  for both (a) incident and (b) reflected waves. (c) The normalized difference in wave celerity  $\bar{c}_w$  is used to compare theoretical and experimental results; (d) the wave amplitude for both incident (dot-dashed line) and reflected (dashed line) waves. Blue empty circles, *KdV-FS*; blue +, *KdV-RL*; black ×, *MCC-RL*; black empty squares, *MCC-FS*.

occurs. The reflected ISW features assume values different from the incident one by virtue of changes in the stratified fluid throw which it propagate. After the propagation of the incident wave packet, indeed, an increase of the upper layer thickness to  $h_1^* > h_1$  occurs. We take into account of this occurrence in our computations, and all quantities associated to reflected ISWs are denoted herein with a superscript asterisk (see Tab. I).

Associated to the interfacial displacement, also surface manifestations occur. The lock gate is quickly lifted up vertically, but its lower edge is left few millimeters deeper than the fluid depth in the ambient region. This allows us to avoid the generation of barotropic surface waves. Those waves, observed for similar experimental procedure in Kodaira *et al.*<sup>33</sup>, propagate faster than the

## The role of the free surface on interfacial solitary waves

internal soliton. Thus, a wave absorber was used to avoid that, once reflected, they could interact with the incoming flow. For all our experiments, we do not observe the generation of surface waves induced by the gate removal. The gray-scale field in the vertical plane  $(y, t)$ , placed at a fixed distance from the lock gate, shows the evolution of both the internal interface and the free surface (Fig. 7c). Before the leading internal wave transition (i.e. for  $t < 1.5$  s), it is not observed any free surface oscillation, and the free surface appears smooth and undisturbed. A packet of short amplitude surface waves passes through the vertical section (i.e. for  $t < 1.5$  s) before and during the ISW leading edge transition. The surface waves packet is composed by four wave crests characterized by comparable amplitudes (of the order of few millimeters) and a decreasing wavelengths as they get closer to the ISW. Kodaira *et al.*<sup>33</sup> observed the generation of those waves for  $\eta_0/h_1 > 1.8$  and  $a_2/h_1 > 0.77$  (with  $\rho_1/\rho_2 = 0.856$ ). In our experiments, we observed their generation for  $\eta_0/h_1 > 1.36$  and  $a_2/h_1 > 0.68$  (with  $\rho_1/\rho_2 = 0.807 \div 0.718$ ). Our lower values are probably due to the larger density difference adopted. The surface small-amplitude waves seem to be transported by the ISW induced velocity field since they propagate with the same internal wave celerity  $c_w$ , until they dissipate. For most of the performed experiments the short surface waves dissipate before or during the ISW reflection, while only for Case 13 they dissipate after their reflection on the right-end wall of the tank.

During all the experiments, a surface displacement having the form of a surface solitary wave, is observed on the free surface above each ISW (see blue line in Fig. 7a). Differently from the short surface waves ahead of it, the surface solitary wave follows the associated interfacial displacement also after its reflection (see Fig. 7c for  $t > 10$  s). The occurrence of such surface deformation is then directly related to the ISW-induced velocity and pressure field.

Features of both the internal and surface manifestations depend on the stratification structures characterizing the lock and the ambient fluid regions. Among all the initial setting parameters, the ISWs amplitude is mostly related to the interfacial displacement  $\eta_0$  (Fig. 8a,c). The latter identifies, indeed, the volume of light fluid initially confined into the lock, below the interface level of the ambient fluid (the lock length and the tank width are kept constant). Although experimental data appear aligned for the incident ISWs, they are ordered again depending on the different initial setting conditions (Fig. 8). Experimental data obtained by Kodaira *et al.*<sup>33</sup> are in good agreement with those obtained in the present work (see green circles in Fig. 8a). They used  $\delta_0 > 0$  and  $\rho = 0.9$ , thus they are placed between cases without  $\delta_0$  (red squares) and those with  $\delta_0 > 0$  and  $\rho = 0.8$  (blue triangles and ciano stars), confirming ours results reliability.



## The role of the free surface on interfacial solitary waves

Unlike the ISWs amplitude, the dimensionless ISW celerity mostly depends on the density structure of the stratified system, rather than the initial interface displacement (Fig. 8b,d for incident and reflected ISWs, respectively). This evidence appears even more clear for reflected ISWs, whose celerity very slightly increases with the wave amplitude. Interestingly, the presence/absence of the initial surface displacement  $\delta_0$  does not imply relevant changes in the waves features. However, ISWs generated with  $\delta_0 > 0$  propagate slightly faster and, consequently present larger interfacial amplitudes. For a given initial interfacial displacement  $\eta_0$ , the ISW amplitude  $a_2$  depends on the ambient fluid structure, i.e. layers thickness and density<sup>16</sup>. The presence of a volume of light fluid within the lock, inducing a surface displacement  $\delta_0$  with respect to the water level of the ambient fluid, brings the ISWs generation mechanism closer to a steady release than an impulsive input. As well as  $\eta_0$ , it acts as a further forcing.

## IV. COMPARISON OF THEORETICAL AND EXPERIMENTAL RESULTS

We compare all the incident and reflected ISWs features with those resulting from mathematical models. Internal waves profile and celerity predicted by the weakly non-linear *KdV* model and by the strongly non-linear *MCC* model are evaluated (Fig. 9). For each, we implement both the rigid lid and the free surface boundary conditions, in order to investigate how the presence of the top free surface affects flow dynamics.

The relationship between normalized ISW speed and amplitude shows that wave celerity estimated for Case 11 by the *MCC-FS* model is very close to the one observed experimentally, both for the incident (Fig. 9c) and for the reflected wave (Fig. 9d). For larger amplitude, as the one measured for the incident ISW, the wave speed is much more overestimated by weakly nonlinear models. Moreover, the wave profile of the rightward-propagating ISW (Case 11), consistently shows good agreement with the *MCC-FS* model (Fig. 9a). Although the wave profile appears slightly asymmetric, the experimental points of both the leading interface (on the right) and the trailing one (on the left) almost lie on the curve predicted by the strongly non-linear model, with a free surface boundary condition. Consistently with that, also the predicted ISW-induced maximum surface displacement shows good agreement with the experimental data. To improve figure readability we show in Figs. 9a, b only the maximum surface displacements inferred from image analysis). After reflection on the right-hand wall of the tank, the wave partially dissipates, and a slight increase

# The role of the free surface on interfacial solitary waves

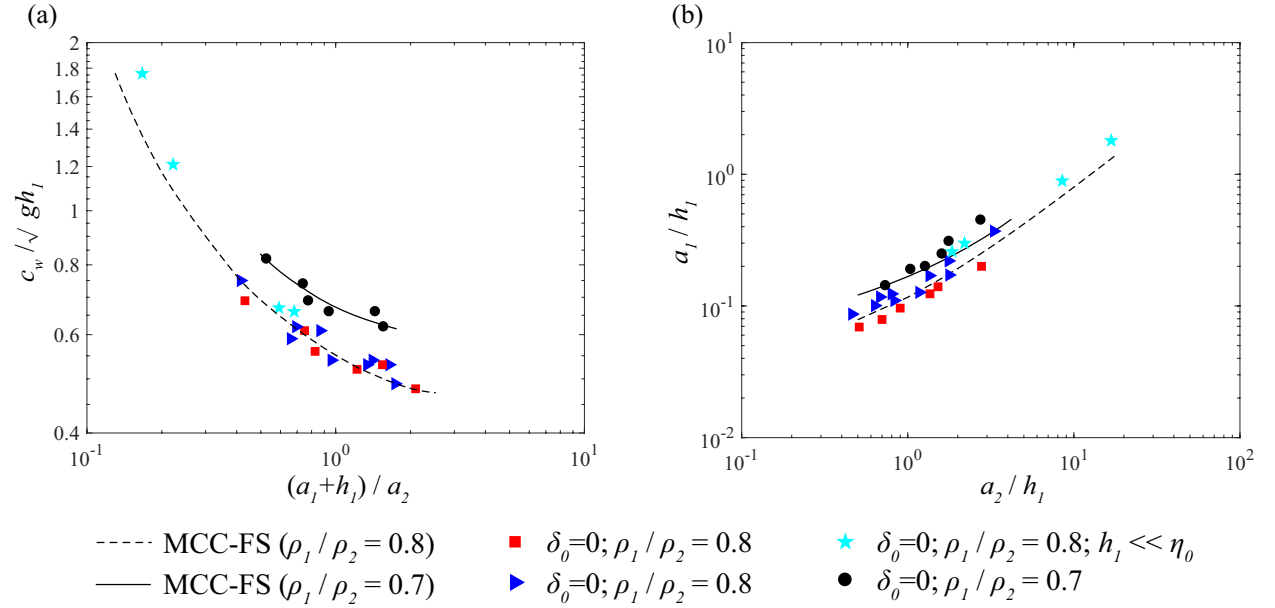


FIG. 11. (a) The ratio  $(a_1 + h_1)/a_2$  is related to the measured celerity, normalized by  $\sqrt{g h_1}$ . (b) Comparison between the measured ISWs amplitudes  $a_2$  and the associated maximum surface displacements  $a_1$ , both non-dimensionalized by using the top layer thickness  $h_1$ . Incident as well as reflected ISWs are shown. Experimental data are shown in logarithmic scales for both the x- and the y-axis. Each mark refers to a defined initial setting condition, defined in the figure legend. Dashed and solid lines approximate results obtained by the *MCC-FS* model for  $\rho$  equal to 0.7 and 0.8, respectively.

of the upper layer thickness occurs ( $h_1^* > h_1$ ). The reflected wave propagating through the vertical cross section placed at  $L_0/2$  away from the lock gate, shows indeed lower amplitude (Fig. 9b). Again, the maximum surface displacement is well predicted by the *MCC-FS* model. Nevertheless, being the wave smaller, the interface profile agrees well with the solitary wave solution of the weakly nonlinear *KdV* model, in accordance with results obtained by<sup>33</sup> for the smallest wave case. More properly, the *KdV-FS* model underestimates the interfacial displacement, which is better predicted by the weakly non-linear model with rigid-lid boundary condition. Although limited to only one case, those preliminary results suggest that the *MCC-FS* model appears the one able to better predict the ISW celerity and the free surface displacement. The prediction of the ISW profile, instead, seems to be related to the wave amplitude: for larger interface profiles, the strongly non-linear the *MCC-FS* model should be implemented.

To compare theoretical and experimental interface profiles, at the interface mid-depth, we evaluate the horizontal distance from the wave trough, for both experimental and theoretical ISW profiles

The role of the free surface on interfacial solitary waves

(i.e.,  $d_e$  and  $d_m$ , respectively). The normalized displacement between theoretical and experimental wave profiles is defined as (see Fig. 9a):

$$\bar{\lambda}_w = \frac{d_m - d_e}{d_e} \quad (24)$$

Experimental interfacial profiles are characterized by  $\bar{\lambda}_w = 0$ . To take into account the ISWs asymmetry, we consider the leading edge of each ISW as representative for the estimation of  $\bar{\lambda}_w$  (i.e., the right and left tail for the incident and reflected ISWs, respectively). Positive (negative) values of  $\bar{\lambda}_w$  are associated to theoretical interface profiles larger (smaller) than the experimental ones. For each Case, we estimate the wave profile displacements  $\bar{\lambda}_w$  both for incident and for reflected waves (Figs. 10a and b, respectively). Except for Case 1, the *MCC-FS* model provides the better prediction for incident waves profile, although  $\bar{\lambda}_w$  is overestimated. The wave profiles resulting from a the strongly nonlinear model implementing a rigid lid condition are the widest provided among all considered mathematical models. The *KdV* models, instead, always predict tighter interfacial profiles, especially for larger ISWs. This occurrence is observed for cases  $3 \div 5$ ,  $6 \div 8$  and  $11 \div 13$ , characterized by an increasing amplitude (Figs. 10a, c). Unlike the *MCC* model, the *KdV* theory provides better results with the rigid lid approximation, rather than with the top free surface.

As a consequence of waves reflection on the right lateral wall of the tank, ISWs partially dissipate, assuming lower amplitudes. Again, for most cases the *MCC-FS* interfacial profiles are the closest to the one observed experimentally. However, for small-amplitude ISWs also the *KdV-RL* theory provides good predictions (see cases 1, 3, 4, 6 and 11 in Figs. 10a, c).

With a similar approach used for the wave profiles, the ISWs celerity evaluated experimentally ( $c_{w,e}$ ), are compared with those predicted by theoretical models ( $c_{w,m}$ ). The dimensionless celerity difference  $\bar{c}_w$  is introduced. It is given by:

$$\bar{c}_w = \frac{|c_{w,m} - c_{w,e}|}{c_{w,e}} \quad (25)$$

For each case, positive values of  $\bar{c}_w$  are associated to rightward propagating ISWs, while negative values refer to reflected waves (Fig. 10c). Our results show that *MCC* theory provides the best prediction for both incident and reflected ISWs. The top free surface and the rigid lid conditions approximately give the same wave speed, with a deviation of 10%. Within this approximation, we can conclude that the wave celerity is mostly affected by the wave amplitude rather than by the surface manifestations. However, the *MCC-FS* model predicts celerities closer to the ones

## The role of the free surface on interfacial solitary waves

observed experimentally, as shown in Figs. 9c, d.

Further investigations on ISWs features observed experimentally, compared with those resulting from the *MCC-FS* model, significantly point out that flow features are better predicted by the strongly non-linear model associated with a top free surface condition. In particular, we investigate how the ISWs celerity is related to the ratio between the largest distance between the free surface and the undisturbed interface  $a_1 + h_1$  and the internal amplitude  $a_2$  (Fig. 11a). Moreover, the relation between the normalized interfacial amplitude  $a_2/h_1$  and surface displacement  $a_1/h_1$  is analyzed (Fig. 11b). For each density ratio, theoretical results are shown by means of interpolating functions (see dashed line for  $\rho=0.8$  and solid line for  $\rho=0.7$  in Fig. 11a).

Cases characterized by the same density ratio show a nonlinear behavior: the wave celerity increases faster than the wave amplitude (Fig. 11a). This suggests that the contribution of the surface displacement in decreasing the wave speed fades the more ISWs show larger interfacial amplitudes. Nevertheless, increasing surface amplitudes are observed as the maximum interfacial displacements become larger (Fig. 11b). However, the internal wave amplitude is always one order of magnitude larger than the associated surface manifestations, and variation of the first affects relatively more the wave speed. We argued the same conclusion analyzing the *MCC-FS* mathematical limits for ISWs interfacial and surface displacements (Fig. 4a).

Interestingly, data appear aligned depending on the different initial setting conditions. As expected, a relative increase of the surface amplitudes  $a_2$  are associated to stratified systems characterized by a larger density difference (see black solid circles for  $\rho = 0.7$  in Fig. 11b). Among the experiments characterized by the same density ratio  $\rho = 0.8$ , cases without the initial surface displacement  $\delta_0$  are characterized by lower surface amplitudes (red squares in Fig. 11b). Thus, the density difference and the additional light fluid in the lock, act in the same way, inducing larger surface manifestations.

## V. DISCUSSION AND CONCLUSIONS

Large amplitude internal solitary waves have been studied experimentally in a system of two fluids, Vaseline oil and salty water, obtaining density ratios in between the Boussinesq and non-Boussinesq flow conditions. We obtained consequently pronounced surface displacements, which in turn affect flow features.

## The role of the free surface on interfacial solitary waves

By image analysis, the main ISWs geometric and kinematic feature are estimated. The initial setting parameters affect the generated solitary wave features and surface manifestations. The presence of a volume of light fluid within the lock, inducing a surface displacement  $\delta_0$  with respect to the water level of the ambient fluid, brings the ISWs generation mechanism closer to a steady release than an impulsive input. This parameter acts inducing slightly larger surface manifestations and internal wave geometric and kinematic features. The latter mostly depends on the volume of light-fluid released. In particular the ISWs amplitude is directly related to the internal displacement  $\eta_0$ , initially produced between the lock and the ambient fluid region. Interestingly, the increase of the density ratio characterizing the undisturbed stratification, affects more the wave celerity rather than the interfacial amplitude, producing more pronounced surface displacements. Approaching to the non Boussinesq conditions, the ISWs-induced velocity and pressure fields, obtained in the small scale apparatus, become closer to those developing in the coastal ocean where packet of internal solitary waves propagate.

Experimental results are compared with those provided by weakly non-linear and strongly non-linear models by considering both rigid lid and free surface as boundary condition at the top. We develop a new mathematical approach to derive the free surface displacement associated to a well-defined ISW propagating in a two-layer stratified system. Our results are similar to those obtained by Barros and Gavriluk<sup>39</sup>. Our approach is based on an analogy with the *MCC-RL* and *KdV* model and valid for single-humped interfacial solitons. It allows to obtain all the solitary wave features once the density structure and the interfacial amplitude are known, leading to interesting theoretical predictions of the free surface. In our cases, each internal solitary wave modelled with a top free surface is always narrower and slower than one resulting from a rigid lid condition. The presence of a free surface become relevant for strongly-stratified two-fluid systems, although it does not affect results for smooth density differences. Moreover, the *MCC* models better describe the wave profile for ISWs with a larger amplitude, since model equations present strongly nonlinear terms.

The analysis of the limiting interfacial amplitudes shows that the density structure strongly affects the elevation of the free surface predicted by the *MCC* model. The free surface maximum displacements increased mostly with the density ratio, and the layers thickness. Larger free surface displacements were observed for cases with a thinner upper layer thickness, since the ISW flow field propagated closer to the free surface. The *MCC-FS* model gives the best prediction in terms of both internal waves geometric/kinematic features and surface displacements. The latter

## The role of the free surface on interfacial solitary waves

act transferring part of the internal wave energy to the free surface leading the waves celerity to assume lower values with respect to those resulting from the *MCC-RL* model. Experimental evidences and theoretical results show that the celerity of an internal solitary wave of depression depends on both interfacial and surface displacement, although they act in opposite way. In particular, an ISW propagates faster if endowed with a larger interfacial amplitude, while the surface manifestation contributes to decrease the wave speed. Surprisingly, the latter behavior fades as waves assume larger internal amplitudes. For decreasing upper layer thicknesses, indeed, the free surface displacements do not grow proportionally to the interfacial amplitudes, and, consequently the *MCC-RL* and the *MCC-FS* celerity predictions tend to converge. This is also confirmed by the theoretical limits for wave geometric features resulting from the *MCC-FS* model. Predictions of the (*KdV-RL*) equation are consistent with experimental results for small-amplitude waves, mostly observed after reflection. Thus, the reliability of a free top surface as boundary condition depends on the wave amplitude and on the density difference. Our theoretical analysis highlights that, under Boussinesq conditions, very good predictions of ISWs features are provided also by the *MCC-RL* model, both for very large and for small amplitude ISWs.

The large amplitude ISWs observed in the Strait of Messina (Mediterranean Sea) propagate in a two-fluid system characterized by a smooth density difference, i.e.,  $\rho_1/\rho_2 \sim 0.99$ ,  $a_2/h_1 \sim 1.7$ ,  $L_w \sim 800\text{m}^{10,43}$ . Under those conditions both the *MCC-FS* and the *MCC-RL* model predict a wave profile very similar to the one resulting from a rigid lid condition (as in Fig. 2d). In particular, to an internal displacement of approximately 50 m a surface displacement of about 4 cm is predicted by the *MCC-FS* model. Consistently with our results, the presence of the free surface does not significantly affect flow features for ISWs characterized by relatively large amplitudes propagating in a stratified ambient fluid with a small density difference. By satellite it is not possible to capture such a small surface slope. SAR images thus show only the existence of short surface waves caused by variations of the short-scale sea surface roughness due to their interaction with a variable surface current.



The role of the free surface on interfacial solitary waves

## Appendix

The continuity and momentum equations for each layers can be written as:

$$\left\{ \begin{array}{l} \frac{\partial \eta_1}{\partial t} + \frac{\partial(u_1 \eta_1)}{\partial x} = 0 \\ \frac{\partial \eta_2}{\partial t} + \frac{\partial(u_2 \eta_2)}{\partial x} = 0 \\ \frac{\partial u_1}{\partial t} + u_1 \frac{\partial u_1}{\partial x} + g \frac{\partial(\eta_1 + \eta_2)}{\partial x} = \frac{1}{\eta_1} \frac{\partial}{\partial x} \left( \frac{1}{3} \eta_1^3 G_1 - \frac{1}{2} \eta_1^2 D_1^2 \eta_2 \right) \\ \quad + \left( \frac{1}{2} \eta_1 G_1 - D_1^2 \eta_2 \right) \frac{\partial \eta_2}{\partial x} \\ \frac{\partial u_2}{\partial t} + u_2 \frac{\partial u_2}{\partial x} + g \frac{\partial(\rho_1 \eta_1 / \rho_2 + \eta_2)}{\partial x} = \frac{1}{\eta_2} \frac{\partial}{\partial x} \left( \frac{1}{3} \eta_2^3 G_2 \right) \\ \quad + \frac{\rho_1}{\rho_2} \frac{\partial}{\partial x} \left( \frac{1}{2} \eta_1^2 G_1 - \eta_1 D_1^2 \eta_2 \right) \end{array} \right. \quad (\text{A.1})$$

where  $u_i = u_i(x, t)$  are the depth-averaged horizontal velocity and  $G_i$  and  $D_i$  ( $i = 1, 2$ ) are non-linear differential operators defined as :

$$G_i \equiv \frac{\partial^2 u_i}{\partial x \partial t} + u_i \frac{\partial^2 u_i}{\partial x^2} - \left( \frac{\partial u_i}{\partial x} \right)^2 = -\frac{1}{\eta_i} (D_i^2 \eta_i). \quad (\text{A.2})$$

The coefficients of differential system (13) are given by:

$$\left\{ \begin{aligned}
 \alpha_{11} &\equiv \frac{c^2 h_1^2}{3\eta_1}, \alpha_{12} \equiv \frac{c^2 h_1^2}{2\eta_1}, \alpha_{13} \equiv -\frac{c^2 h_1^2}{6\eta_1^2}, \alpha_{14} \equiv \frac{c^2 h_1^2}{2\eta_1^2}, \alpha_{15} \equiv 0 \\
 \alpha_{16} &\equiv -g(\eta_1 + \eta_2 - h_1 - h_2) + \frac{c^2}{2} \left(1 - \left(\frac{h_1}{\eta_1}\right)^2\right) \\
 \alpha_{21} &\equiv \frac{\rho c^2 h_1^2}{2\eta_1}, \alpha_{22} \equiv \frac{\rho c^2 h_1^2}{\eta_1} + \frac{c^2 h_2^2}{3\eta_2}, \alpha_{23} \equiv -\frac{\rho c^2 h_1^2}{2\eta_1^2} \\
 \alpha_{24} &\equiv -\frac{c^2 h_2^2}{6\eta_2^2}, \alpha_{25} \equiv -\frac{\rho c^2 h_1^2}{\eta_1^2} \\
 \alpha_{26} &\equiv -g(\rho\eta_1 + \eta_2 - \rho h_1 - h_2) + \frac{c^2}{2} \left(1 - \left(\frac{h_2}{\eta_2}\right)^2\right) \\
 \alpha_{31} &\equiv \frac{\rho c^2 h_1^2}{6} \left(2 + 3\frac{\eta_2}{\eta_1}\right), \alpha_{32} \equiv \frac{c^2 h_1^2}{6} \left(2 + 3\rho\frac{h_1^2}{h_2^2} \left(1 + 2\frac{\eta_2}{\eta_1}\right)\right) \\
 \alpha_{33} &\equiv -\frac{\rho c^2 h_1^2}{6\eta_1} \left(2 + 3\frac{\eta_2}{\eta_1}\right), \alpha_{34} \equiv -\frac{c^2 h_2^2}{3\eta_2} \\
 \alpha_{35} &\equiv -\frac{\rho c^2 h_1^2}{2\eta_1} \left(1 + 2\frac{\eta_2}{\eta_1}\right) \\
 \alpha_{36} &\equiv \rho c^2 h_1 \left(1 - \frac{h_1}{\eta_1}\right) + c^2 h_2 \left(1 - \frac{h_2}{\eta_2}\right) - \\
 &\frac{1}{2}g \left[ \rho\eta_1^2 \left(1 - \frac{h_1^2}{\eta_1^2}\right) + 2\rho\eta_1\eta_2 \left(1 - \frac{h_1}{\eta_1} \frac{h_2}{\eta_2}\right) + \eta_2^2 \left(1 - \frac{h_2^2}{\eta_2^2}\right) \right] \\
 \alpha_{41} &\equiv \frac{\rho c^3 h_1^2}{6} \left[ 2\left(1 - \frac{h_1}{\eta_1}\right) + 3\frac{\eta_2}{\eta_1} \left(1 - \frac{h_2}{\eta_2}\right) \right] \\
 \alpha_{42} &\equiv \frac{c^3 h_1^2}{6} \left[ 3\rho - 3\rho\left(\frac{h_1}{\eta_1} + 2\frac{h_2}{\eta_1} - 2\frac{\eta_2}{\eta_1}\right) + 2\frac{h_2^2}{h_1^2} - 2\frac{h_2^3}{h_1^2\eta_2} \right] \\
 \alpha_{43} &\equiv -\frac{\rho c^3 h_1^2}{6\eta_1} \left(2 + 3\frac{\eta_2}{\eta_1} - \frac{h_1}{\eta_1} - 3\frac{h_2}{\eta_1}\right) \\
 \alpha_{44} &\equiv -\frac{c^3 h_2^2}{6\eta_2} \left(2 - \frac{h_2}{\eta_2} + 3\rho\frac{h_1^2}{h_2^2} \frac{h_1}{\eta_1} \frac{\eta_2}{\eta_1}\right) \\
 \alpha_{45} &\equiv -\frac{\rho c^3 h_2^2}{2\eta_1} \frac{h_1^2}{h_2^2} \left(1 - 2\frac{h_2}{\eta_1} + 2\frac{\eta_2}{\eta_1}\right) \\
 \alpha_{46} &\equiv \frac{c}{2} \left(\eta_2 \left(1 - \frac{h_2}{\eta_2}\right)^2 \left(c^2 \frac{h_2}{\eta_2} - g\eta_2\right) + \right. \\
 &\left. \rho \left(1 - \frac{h_1}{\eta_1}\right) \left(c^2 \frac{h_1}{\eta_1} (\eta_1 - h_1) + gh(h_1 + 2h_2 - \eta_1 - 2\eta_2)\right) \right)
 \end{aligned} \right. \quad (\text{A.3})$$

## The role of the free surface on interfacial solitary waves

The coefficients  $\beta_j$  ( $j = 1, 2, 3, 4$ ) are defined as:

$$\left\{ \begin{array}{l} \beta_1 \equiv \rho c^2 h_1^2 \eta_2 \\ \beta_2 \equiv c^2 (h_2^2 \eta_1 + 3\rho h_1^2 \eta_2) \\ \beta_3 \equiv 3\rho c^2 h_1^2 \eta_2 \\ \beta_4 \equiv -3c^2 (\eta_1 (\eta_2 - h_2)^2 + \rho \eta_2 (\eta_1 - h_1)^2) \\ \quad + 3g\eta_1 \eta_2 ((\eta_2 - h_2)^2 \\ \quad + \rho (\eta_1 - h_1)^2 + 2\rho (\eta_1 - h_1)(\eta_2 - h_2)) \end{array} \right. \quad (\text{A.4})$$

## REFERENCES

- <sup>1</sup>C. Jackson, “Internal wave detection using the moderate resolution imaging spectroradiometer (MODIS),” *Journal of Geophysical Research: Oceans* **112** (2007).
- <sup>2</sup>T. Maxworthy, “A note on the internal solitary waves produced by tidal flow over a three-dimensional ridge,” *Journal of Geophysical Research: Oceans* **84**, 338–346 (1979).
- <sup>3</sup>A. New and R. Pingree, “Local generation of internal soliton packets in the central Bay of Biscay,” *Deep Sea Research Part A. Oceanographic Research Papers* **39**, 1521–1534 (1992).
- <sup>4</sup>D. Bogucki, T. Dickey, and L. Redekopp, “Sediment resuspension and mixing by resonantly generated internal solitary waves,” *Journal of Physical Oceanography* **27**, 1181–1196 (1997).
- <sup>5</sup>J. Nash and J. Moum, “River plumes as a source of large-amplitude internal waves in the coastal ocean,” *Nature* **437**, 400 (2005).
- <sup>6</sup>Y. Dossmann, F. Auclair, and A. Paci, “Topographically induced internal solitary waves in a pycnocline: Secondary generation and selection criteria,” *Physics of Fluids* **25**, 086603 (2013).
- <sup>7</sup>J. Apel, J. Holbrook, A. Liu, and J. Tsai, “The Sulu Sea internal soliton experiment,” *Journal of Physical Oceanography* **15**, 1625–1651 (1985).
- <sup>8</sup>D. Farmer and L. Armi, “The generation and trapping of solitary waves over topography,” *Science* **283**, 188–190 (1999).
- <sup>9</sup>L. Bordoio, F. Auclair, A. Paci, Y. Dossmann, and C. Nguyen, “Nonlinear processes generated by supercritical tidal flow in shallow straits,” *Physics of Fluids* **29**, 066603 (2017).
- <sup>10</sup>P. Brandt, A. Rubino, D. Quadfasel, W. Alpers, J. Sellschopp, and H. Fiekas, “Evidence for the

## The role of the free surface on interfacial solitary waves

influence of Atlantic–Ionian stream fluctuations on the tidally induced internal dynamics in the Strait of Messina,” *Journal of physical oceanography* **29**, 1071–1080 (1999).

- <sup>11</sup>W. Alpers, P. Brandt, A. Rubino, and J. Backhaus, “Recent contributions of remote sensing to the study of internal waves in the Straits of Gibraltar and Messina,” *Bulletin - Institut Oceanographique Monaco-Numero Special* - , 21–40 (1996).
- <sup>12</sup>G. Carter, M. Gregg, and R.-C. Lien, “Internal waves, solitary-like waves, and mixing on the Monterey Bay shelf,” *Continental Shelf Research* **25**, 1499–1520 (2005).
- <sup>13</sup>G. La Forgia, C. Adduce, F. Falcini, and C. Paola, “Migrating bedforms generated by solitary waves,” *Geophysical Research Letters* **46**, 4738–4746 (2019).
- <sup>14</sup>K. Davis and S. Monismith, “The modification of bottom boundary layer turbulence and mixing by internal waves shoaling on a barrier reef,” *Journal of Physical Oceanography* **41**, 2223–2241 (2011).
- <sup>15</sup>G. la Forgia, T. Tokyay, C. Adduce, and G. Constantinescu, “Numerical investigation of breaking internal solitary waves,” *Physical Review Fluids* **3**, 104801 (2018b).
- <sup>16</sup>B. Sutherland, K. Barret, and G. Ivey, “Shoaling internal solitary waves,” *Journal of Geophysical Research: Oceans* **118**, 4111–4124 (2013).
- <sup>17</sup>T. Benjamin, “Internal waves of finite amplitude and permanent form,” *Journal of Fluid Mechanics* **25**, 241–270 (1966).
- <sup>18</sup>J. Grue, A. Jensen, P.-O. Rusås, and J. Sveen, “Properties of large-amplitude internal waves,” *Journal of Fluid Mechanics* **380**, 257–278 (1999).
- <sup>19</sup>K. R. Khusnutdinova, Y. Stepanyants, and M. R. Tranter, “Soliton solutions to the fifth-order Korteweg–de Vries equation and their applications to surface and internal water waves,” *Physics of Fluids* **30**, 022104 (2018).
- <sup>20</sup>V. Djordjevic and L. Redekopp, “The fission and disintegration of internal solitary waves moving over two-dimensional topography,” *Journal of Physical Oceanography* **8**, 1016–1024 (1978).
- <sup>21</sup>R. Grimshaw, D. Pelinovsky, E. Pelinovsky, and A. Slunyaev, “Generation of large-amplitude solitons in the extended Korteweg–de Vries equation,” *Chaos: An Interdisciplinary Journal of Nonlinear Science* **12**, 1070–1076 (2002).
- <sup>22</sup>M. Stastna and K. G. Lamb, “Large fully nonlinear internal solitary waves: The effect of background current,” *Physics of fluids* **14**, 2987–2999 (2002).
- <sup>23</sup>M. Dunphy, C. Subich, and M. Stastna, “Spectral methods for internal waves: indistinguishable density profiles and double-humped solitary waves,” *Nonlinear Processes in Geophysics* **18**,

# The role of the free surface on interfacial solitary waves

351–358 (2011).

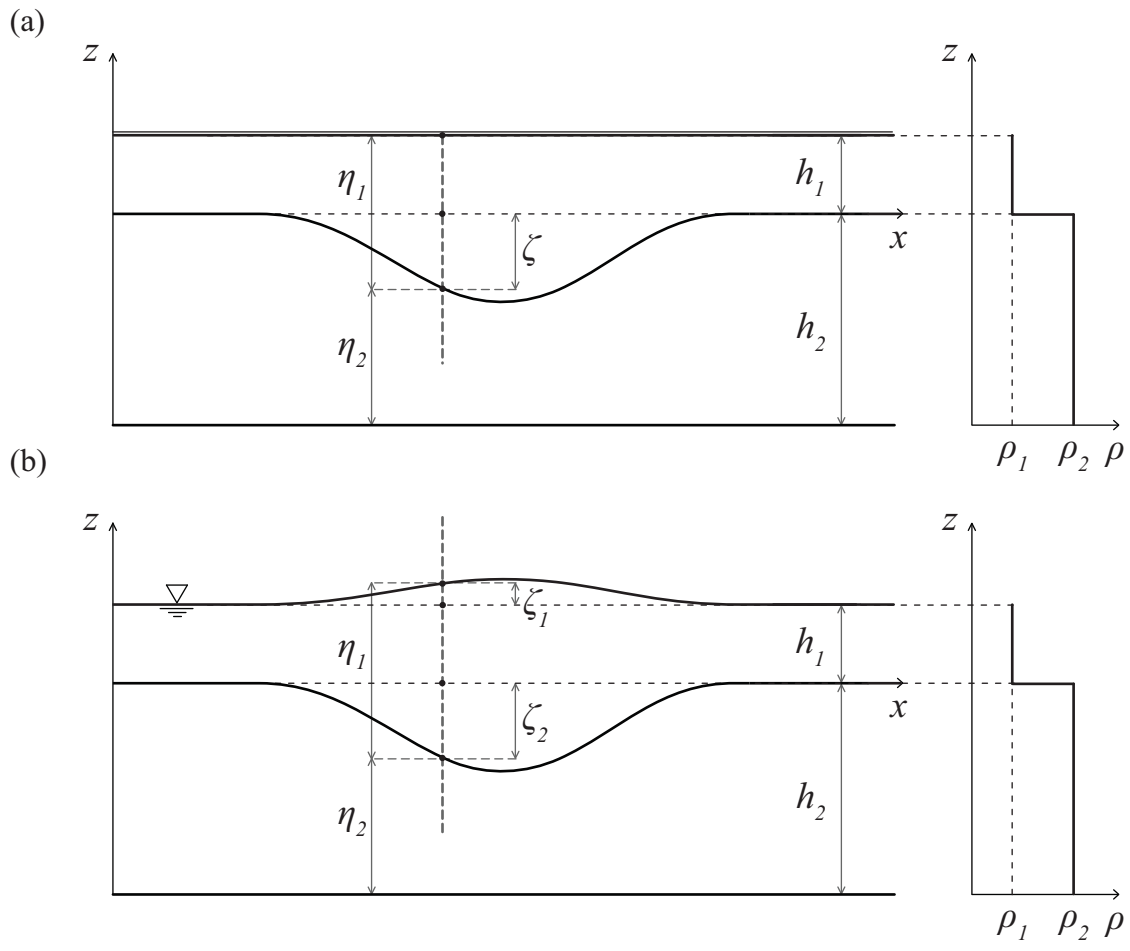
- <sup>24</sup>M. Miyata, “An internal solitary wave of large amplitude,” *La mer* **23**, 43–48 (1985).
- <sup>25</sup>M. Miyata, “Long internal waves of large amplitude,” in *Nonlinear water waves* (Springer, 1988) pp. 399–406.
- <sup>26</sup>W. Choi and R. Camassa, “Fully nonlinear internal waves in a two-fluid system,” *Journal of Fluid Mechanics* **396**, 1–36 (1999).
- <sup>27</sup>H. Michallet and E. Barthelémy, “Experimental study of interfacial solitary waves,” *Journal of Fluid Mechanics* **366**, 159–177 (1998).
- <sup>28</sup>R. Camassa, W. Choi, H. Michallet, P.-O. Rusås, and J. Sveen, “On the realm of validity of strongly nonlinear asymptotic approximations for internal waves,” *Journal of fluid mechanics* **549**, 1–23 (2006).
- <sup>29</sup>L. Ostrovsky and J. Grue, “Evolution equations for strongly nonlinear internal waves,” *Physics of Fluids* **15**, 2934–2948 (2003).
- <sup>30</sup>T. Kao, F.-S. Pan, and D. Renouard, “Internal solitons on the pycnocline: generation, propagation, and shoaling and breaking over a slope,” *Journal of Fluid Mechanics* **159**, 19–53 (1985).
- <sup>31</sup>H. Michallet and G. Ivey, “Experiments on mixing due to internal solitary waves breaking on uniform slopes,” *Journal of Geophysical Research: Oceans* **104**, 13467–13477 (1999).
- <sup>32</sup>G. la Forgia, C. Adduce, and F. Falcini, “Laboratory investigation on internal solitary waves interacting with a uniform slope,” *Advances in Water Resources* **120**, 4–18 (2018a).
- <sup>33</sup>T. Kodaira, T. Waseda, M. Miyata, and W. Choi, “Internal solitary waves in a two-fluid system with a free surface,” *Journal of Fluid Mechanics* **804**, 201–223 (2016).
- <sup>34</sup>W. R. Inc., “Mathematica, Version 11.2,” Champaign, IL, 2017.
- <sup>35</sup>D. Korteweg and G. D. Vries, “On the change of form of long waves advancing in a rectangular canal, and on a new type of long stationary waves,” *The London, Edinburgh, and Dublin Philosophical Magazine and Journal of Science* **39**, 422–443 (1895).
- <sup>36</sup>W. Choi and R. Camassa, “Weakly nonlinear internal waves in a two-fluid system,” *Journal of Fluid Mechanics* **313**, 83–103 (1996).
- <sup>37</sup>R. Barros, S. Gavriluk, and V. Teshukov, “Dispersive nonlinear waves in two-layer flows with free surface. i. model derivation and general properties,” *Studies in Applied Mathematics* **119**, 191–211 (2007a).
- <sup>38</sup>P. Sanchez, “Cnoidal solutions, shock waves, and solitary wave solutions of the improved Korteweg-de Vries equation,” *Romanian Journal of Physics* **60**, 379–400 (2015).

# The role of the free surface on interfacial solitary waves

- <sup>39</sup>R. Barros and S. Gavriluk, “Dispersive nonlinear waves in two-layer flows with free surface part ii. large amplitude solitary waves embedded into the continuous spectrum,” *Studies in Applied Mathematics* **119**, 213–251 (2007b).
- <sup>40</sup>N. Soontiens, M. Stastna, and M. Waite, “Trapped internal waves over topography: Non-Boussinesq effects, symmetry breaking and downstream recovery jumps,” *Physics of Fluids* **25**, 066602 (2013).
- <sup>41</sup>L. Ottolenghi, C. Adduce, R. Inghilesi, F. Roman, and V. Armenio, “Mixing in lock-release gravity currents propagating up a slope,” *Physics of Fluids* **28**, 056604 (2016).
- <sup>42</sup>P. Aghsaee, L. Boegman, and K. G. Lamb, “Breaking of shoaling internal solitary waves,” *Journal of Fluid Mechanics* **659**, 289–317 (2010).
- <sup>43</sup>R. Droghei, F. Falcini, D. Casalbone, E. Martorelli, R. Mosetti, G. Sannino, R. Santoleri, and F. Chiocci, “The role of internal solitary waves on deep-water sedimentary processes: the case of up-slope migrating sediment waves off the Messina Strait,” *Scientific reports* **6**, 36376 (2016).

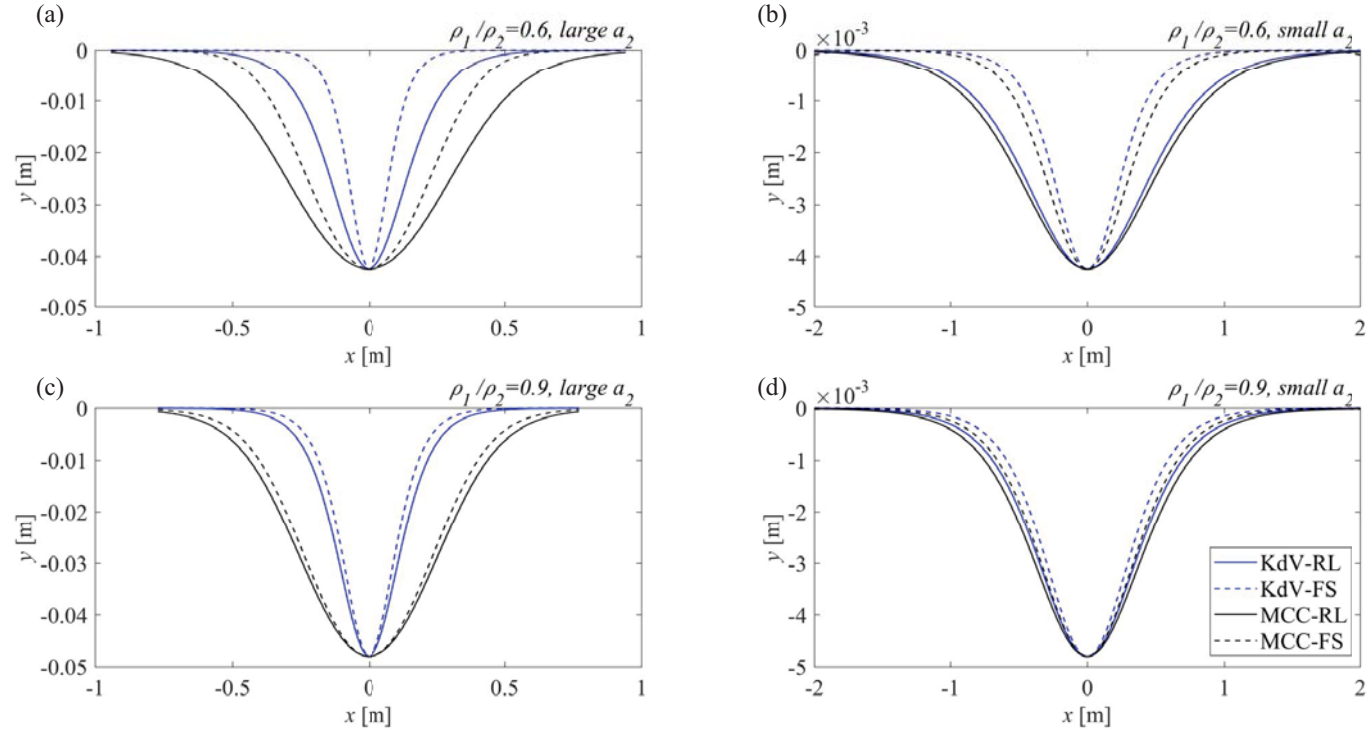


This is the author's peer reviewed, accepted manuscript. However, the online version of record will be different from this version once it has been copyedited and typeset.  
PLEASE CITE THIS ARTICLE AS DOI:10.1063/1.5120621



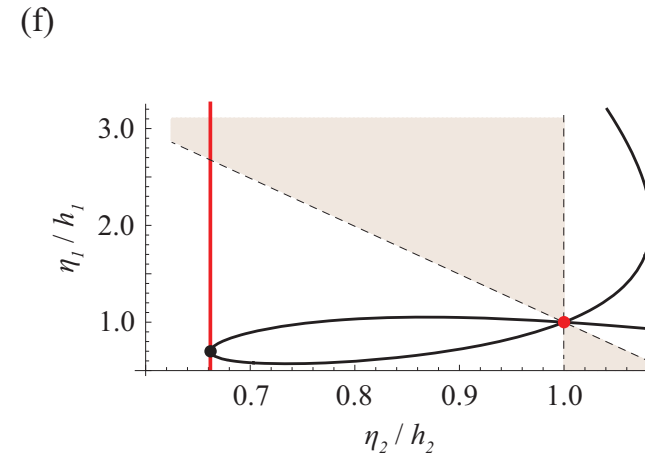
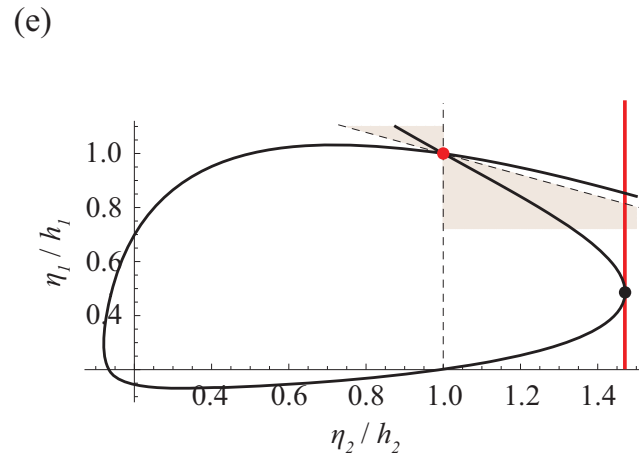
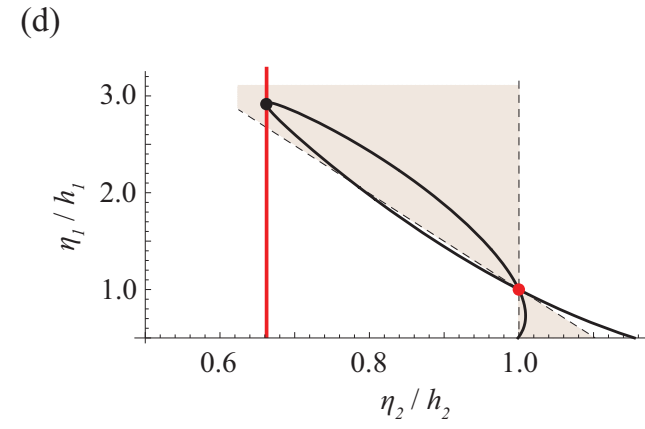
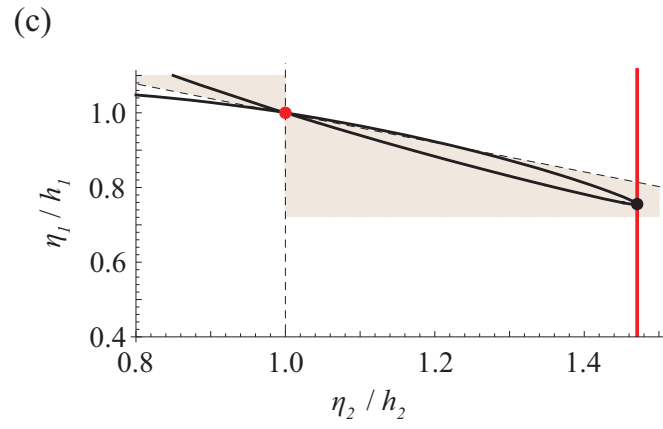
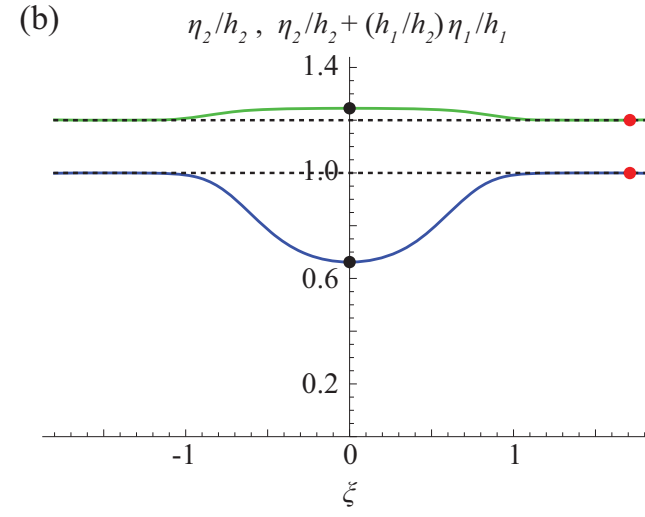
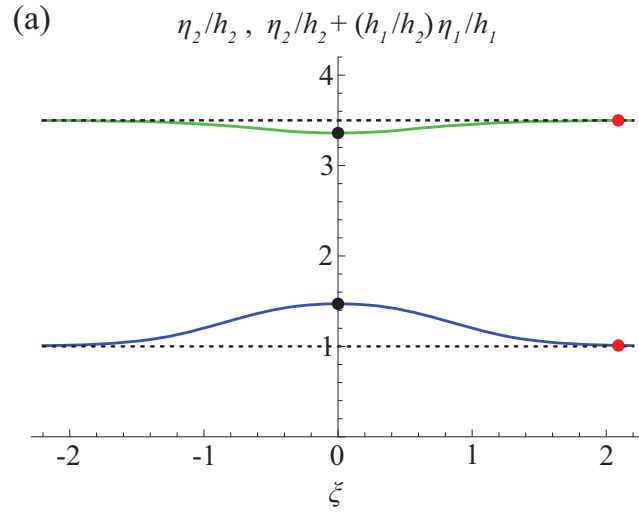
This is the author's peer reviewed, accepted manuscript. However, the online version of record will be different from this version once it has been copyedited and typeset.

PLEASE CITE THIS ARTICLE AS DOI:10.1063/1.5120621



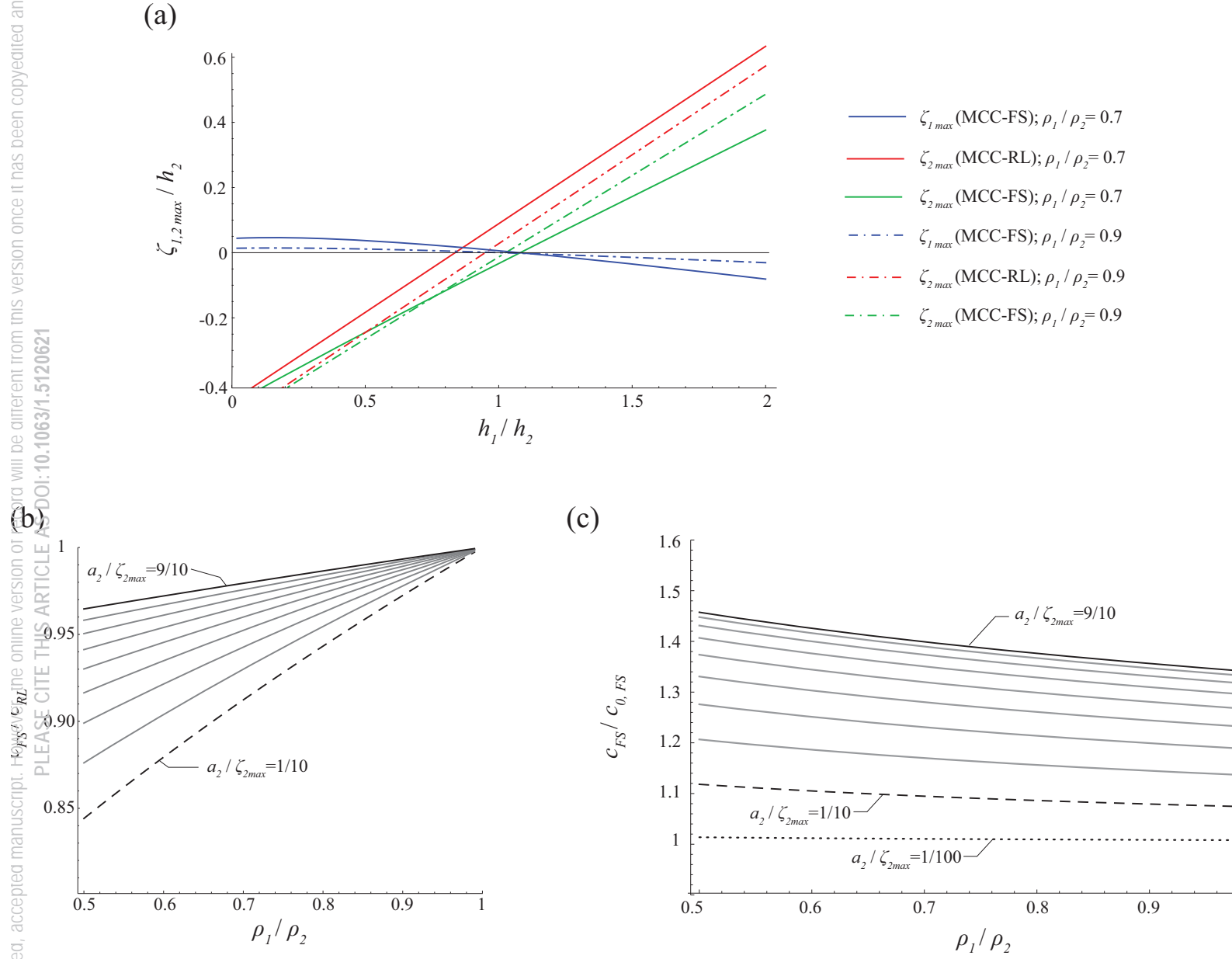
This is the author's peer reviewed, accepted manuscript. However, the online version of record will be different from this version once it has been copyedited and typeset.

PLEASE CITE THIS ARTICLE AS DOI:10.1063/1.5120621

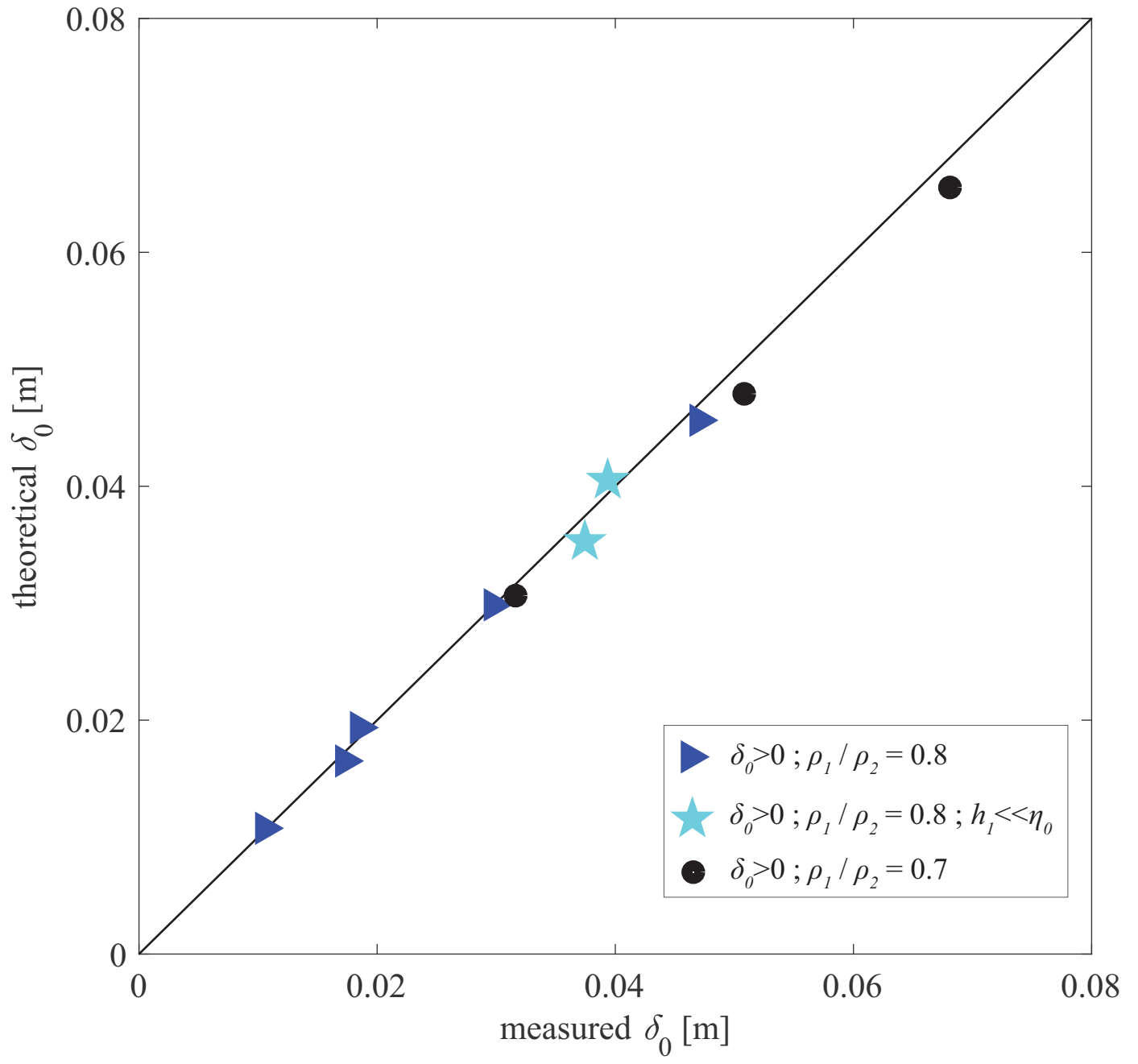


This is the author's peer-reviewed, accepted manuscript. It will be different from this version once it has been copyedited and typeset.

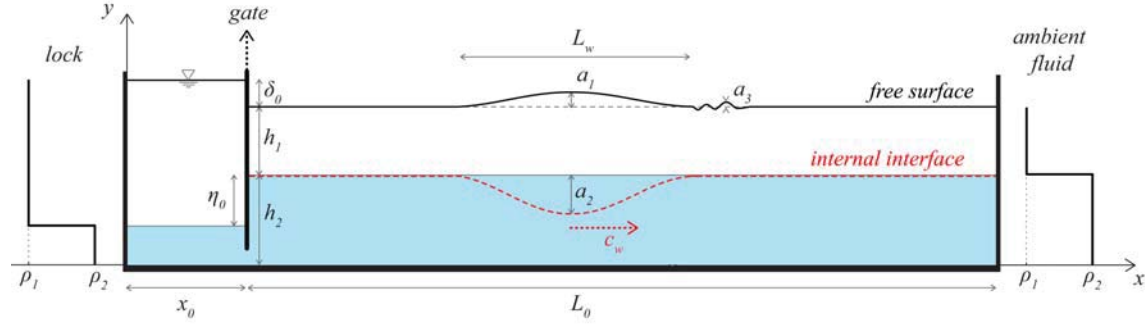
PLEASE CITE THIS ARTICLE AS DOI:10.1063/1.5120621



This is the author's peer reviewed, accepted manuscript. However, the online version of record will be different from this version once it has been copyedited and typeset.  
PLEASE CITE THIS ARTICLE AS DOI:10.1063/1.5120621



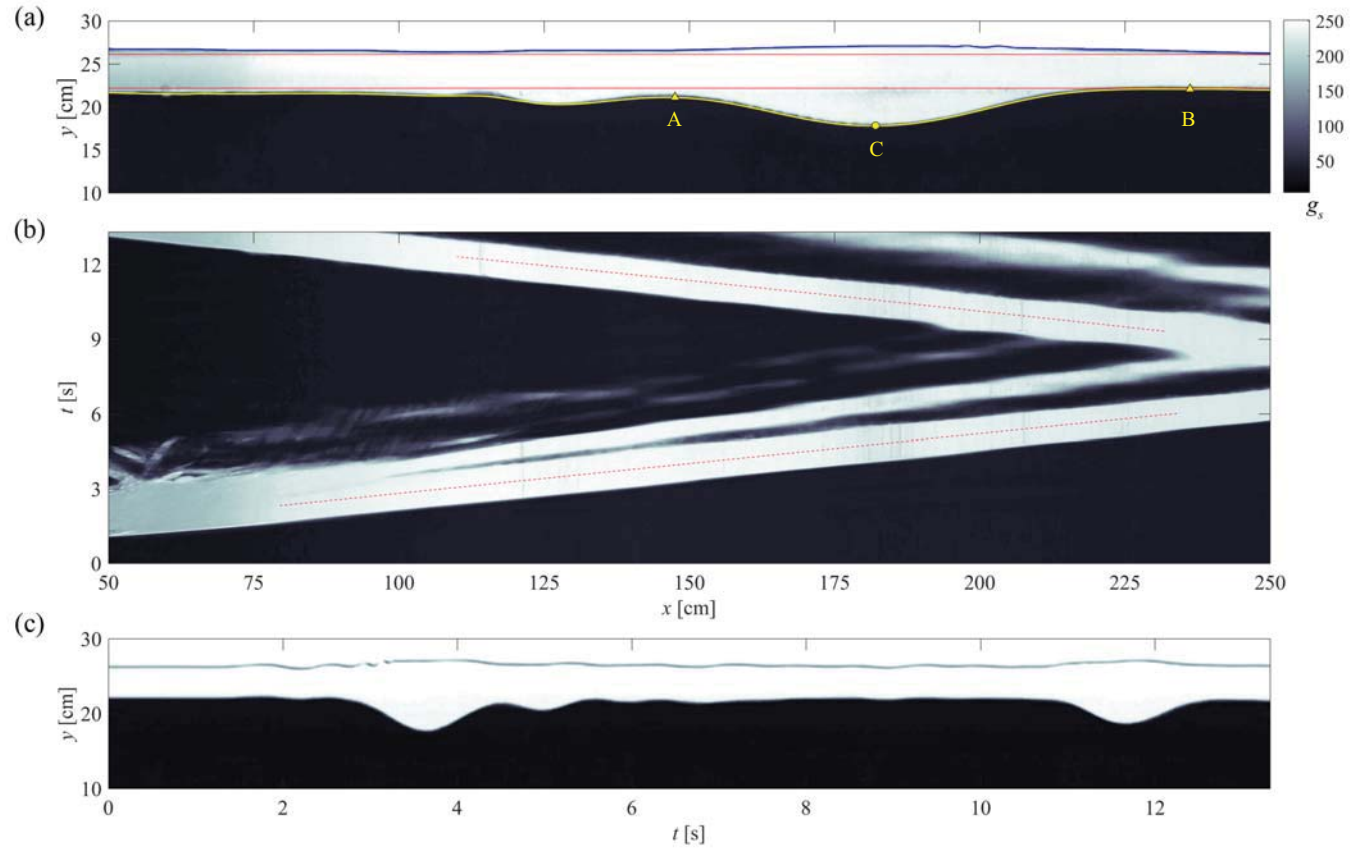
PLEASE CITE THIS ARTICLE AS DOI:10.1063/1.5120621





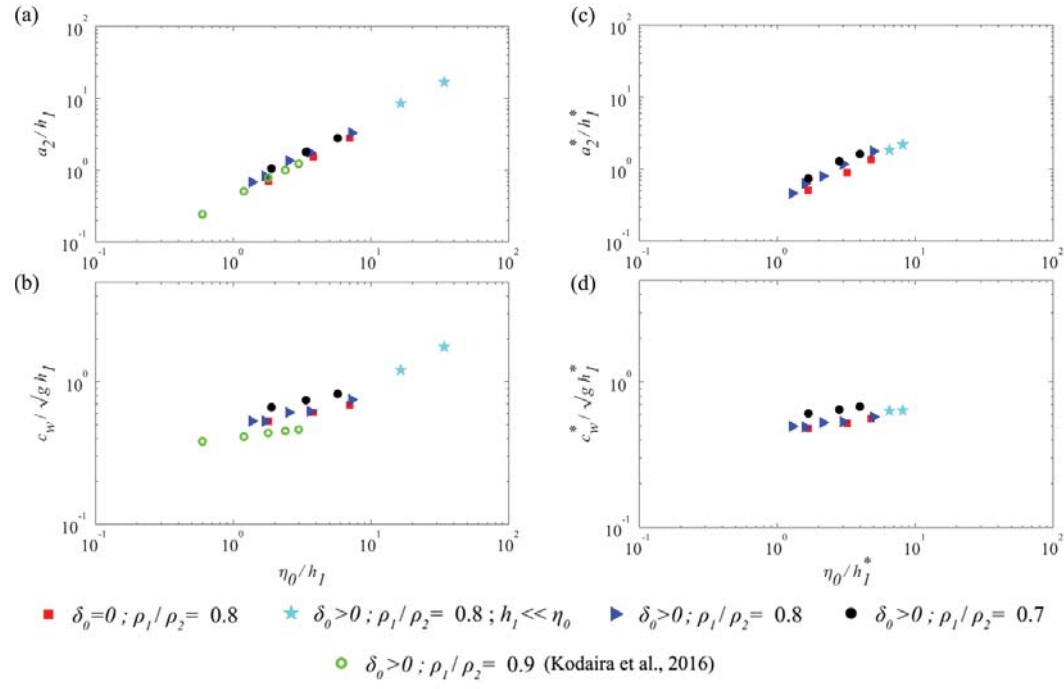
This is the author's peer reviewed, accepted manuscript. However, the online version of record will be different from this version once it has been copyedited and typeset.

PLEASE CITE THIS ARTICLE AS DOI:10.1063/1.5120621



This is the author's peer reviewed, accepted manuscript. However, the online version of record will be different from this version once it has been copyedited and typeset.

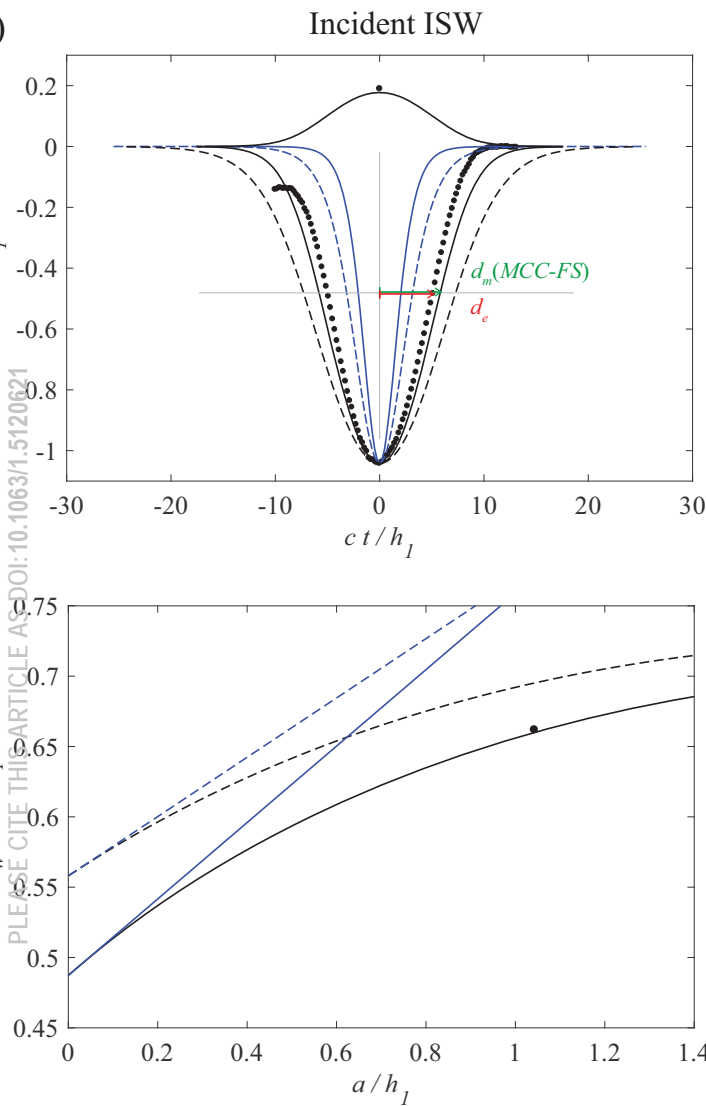
PLEASE CITE THIS ARTICLE AS DOI:10.1063/1.5120621



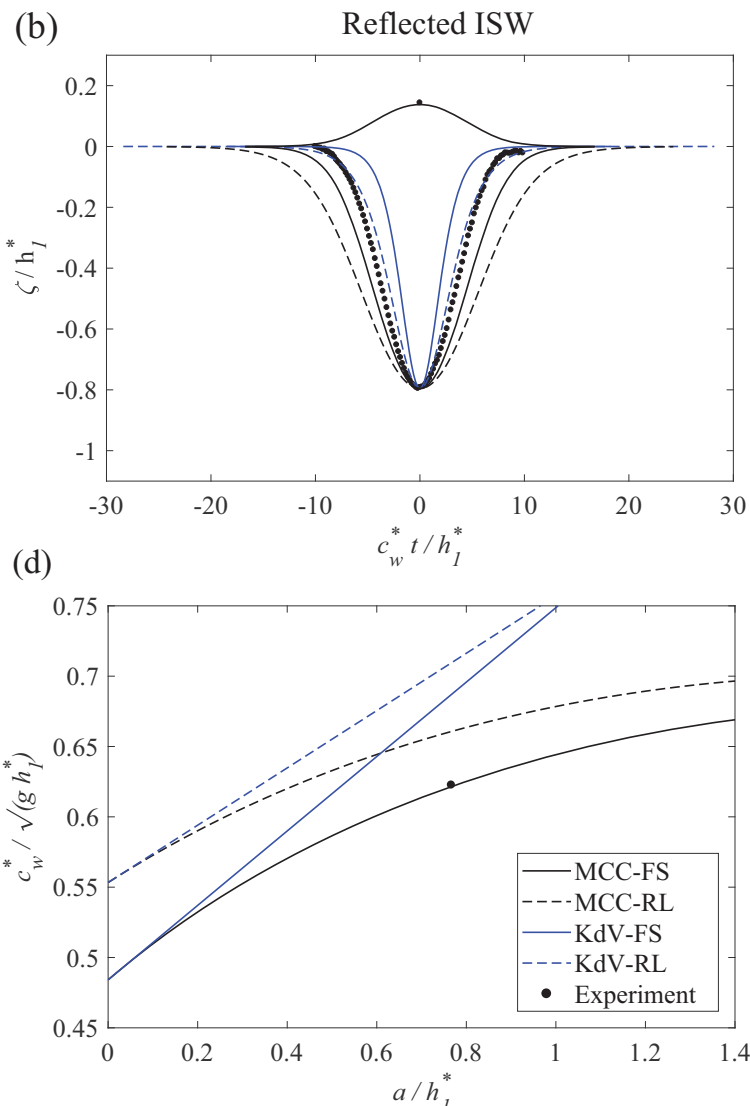
This is the author's peer-reviewed, accepted manuscript. However, the version of record will be different from this version once it has been copyedited and typeset.

PLEASE CITE THIS ARTICLE AS DOI:10.1063/1.5120621

(a)



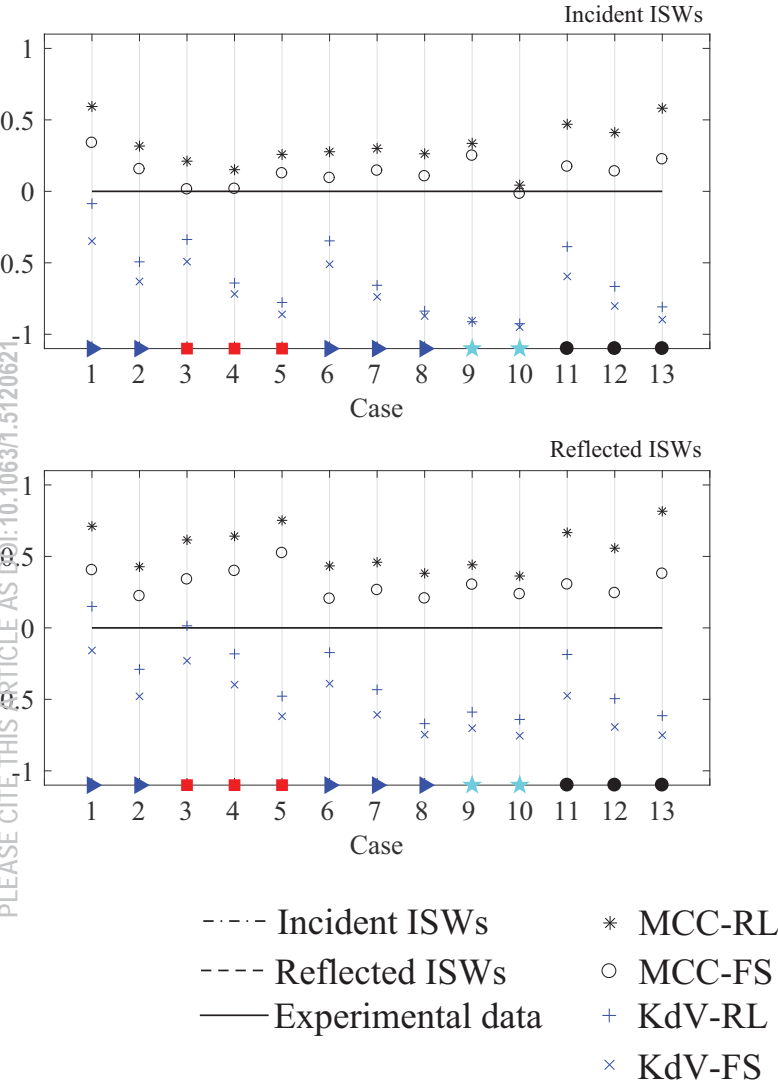
(b)



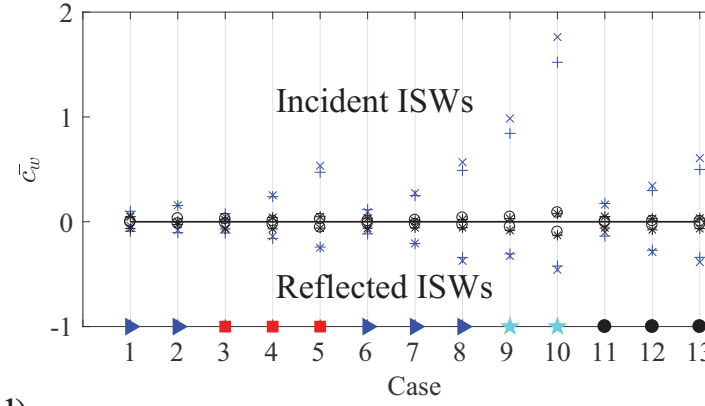
This is the author's peer-reviewed, accepted manuscript. However, the online version of this manuscript will be different from this version once it has been copyedited and typeset.

PLEASE CITE THIS ARTICLE AS DOI:10.1063/1.5120621

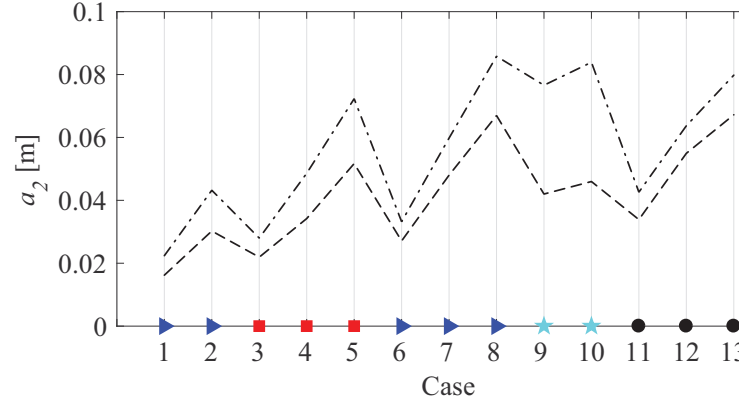
(b)



(c)



(d)

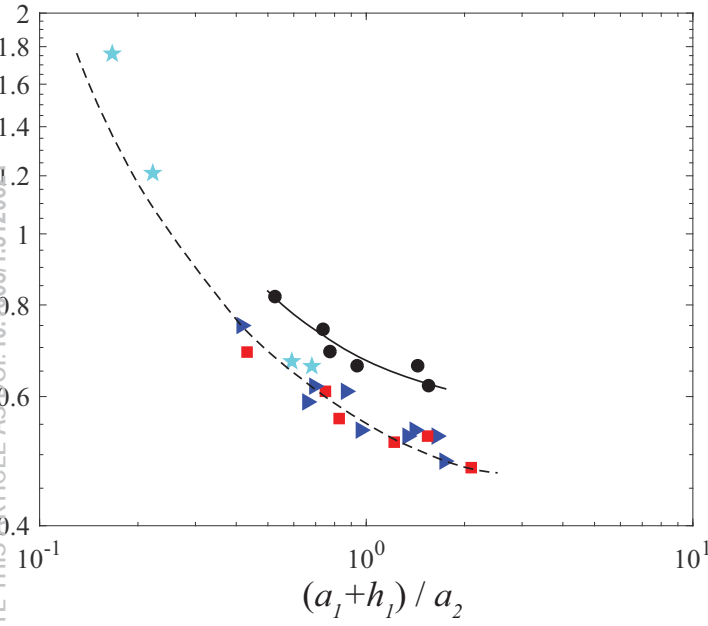


- $\delta_0=0; \rho_1 / \rho_2 = 0.8$
- $\delta_0=0; \rho_1 / \rho_2 = 0.8$
- ★  $\delta_0=0; \rho_1 / \rho_2 = 0.8; h_1 \ll \eta_0$
- $\delta_0=0; \rho_1 / \rho_2 = 0.7$

This is the author's peer reviewed, accepted manuscript. However, the online version of record will be different from this version once it has been copyedited and typeset.

PLEASE CITE THIS ARTICLE AS DOI:10.1063/1.5120621

(a)



----- MCC-FS ( $\rho_1 / \rho_2 = 0.8$ )

———— MCC-FS ( $\rho_1 / \rho_2 = 0.7$ )

■  $\delta_0=0; \rho_1 / \rho_2 = 0.8$

►  $\delta_0=0; \rho_1 / \rho_2 = 0.8$

★  $\delta_0=0; \rho_1 / \rho_2 = 0.8; h_1 \ll \eta_0$

●  $\delta_0=0; \rho_1 / \rho_2 = 0.7$

(b)

